Λ_c Reconstruction with Artificial Neural Networks

Relatore:

Prof. Andrea Alici

Presentata da:

Chiara Fraticelli

Abstract

The ALICE experiment at LHC is dedicated to the study of ultrarelativistic heavy-ion collisions in order to investigate the properties of the Quark-Gluon Plasma (QGP), a phase of matter expected to be formed under extreme energy densities. Probing the QGP is very challenging due to its extremely short lifetime. Heavy quarks produced in initial hard scattering processes are sensitive probes of the medium created in such collisions. The aim of this thesis is to perform a feasibility study on the reconstruction of the Λ_c charm baryon with artificial neural networks. The study is based on a multivariate analysis method which has the advantage of simultaneously considering multiple event properties, exploiting as much of the available information possible through machine learning techniques.

Contents

Introduction

The ALICE (A Large Ion Collider Experiment) experiment, located at the Large Hadron Collider (LHC) at CERN, is dedicated to the study of ultra-heavy relativistic ion collisions. The main objective of the experiment is to investigate the state of matter that is formed under extreme temperature and energy density conditions, known as Quark-Gluon Plasma (QGP). The QGP proves to be difficult to observe and due to its extremely short average lifetime, the proof of its existence is all due to indirect measures. One of the fundamental tools for the investigation of its properties is the study of heavy quarks. In fact, due to their high masses, they are produced in hard scattering the very early stages of the collision and, propagating through the medium, they interact with its constituents throughout the full evolution of the system, thus providing direct measurements on its properties. In particular, in this thesis we studied the charm baryon Λ_c in its decay channel $\Lambda_c^+ \to pK_S^0$. Because of its short average lifetime and low ratio between signal and background, the reconstruction of this particle is complicated, so it is necessary to use multivariate analysis techniques, which allow to consider simultaneously multiple event properties. In this thesis we used the neural networks method to take advantage of all the information available through machine learning techniques.

Chapter 1

Physics of the ALICE experiment

1.1 Introduction to the Standard Model

The Standard Model [1] is the name given in the 1970s to the theory of fundamental particles and how they interact. It describes three of the four known fundamental forces in the universe (the electromagnetic, weak, and strong interactions, and doesn't include the gravitational force), as well as classifying all known elementary particles to date. It is based on quantum field theories, which are able to reconcile the principles of quantum mechanics and special relativity: there is a field corresponding to each particle, that can take on quantized energy states; the particles are the quantum of each respective field when they are in any state other than the fundamental one. Fundamental particles are either the building blocks of matter, fermions, or the interaction mediators, bosons. Fermions obey a statistical rule described by Fermi, Dirac and Pauli called the exclusion principle. Simply stated, fermions cannot occupy the same place at the same time whereas bosons have no problem doing so. More formally, two or more bosons may be described by the same set of quantum numbers. The statistical rules that bosons obey were first described by Bose and Einstein. The Standard Model includes 12 fermions and 4 bosons as shown in figure 1.1. The fermions are divided in 6 quarks and 6 leptons (and their antiparticles), which represent the corresponding fields. The Z^0 and $W^\pm$ bosons are the mediators of the weak interactions while the photon γ is the mediators of the electromagnetic interactions, as are the gluons for the strong ones. The interactions are described using gauge theories: the strong interaction is described by the $SU(3)$ group, which describes the color charge; the electromagnetic one by the group $U(1)$ and the weak one by the group $SU(2)$ and acts on the left-handed particles. If this latter symmetry were correct, the theory would not be renormalizable and the bosons should not have mass, which is instead the case according to experimental evidence. It is therefore necessary to introduce the Higgs mechanism, which explains that bosons and fermions acquire mass through interaction with the Higgs scalar field. Experimental evidence confirms the validity of the Standard Model; this theory, however, cannot yet be considered complete for the lack of an explanation of the gravitational interaction and for the incompatibility with the principles of general relativity.
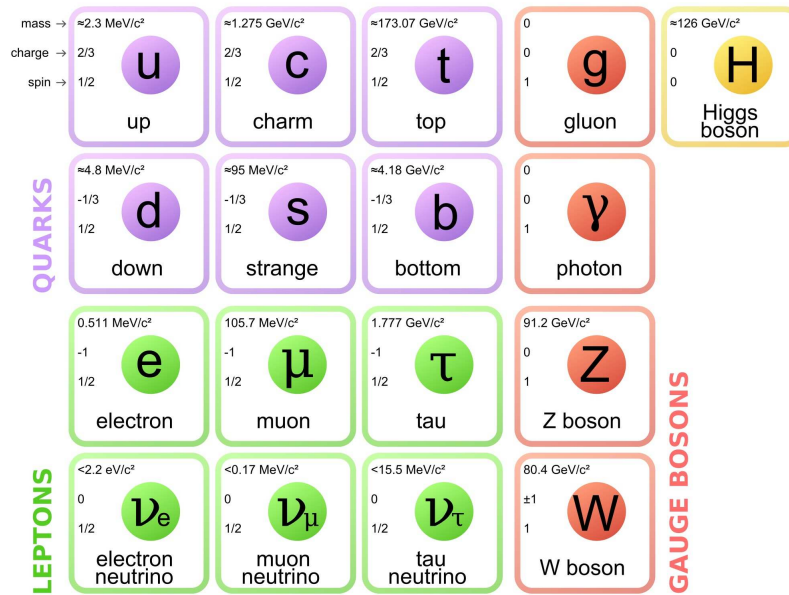
Figure 1.1: Standard Model of elementary particles: quarks and leptons, that form ordinary matter, gauge bosons, interaction mediators and the Higgs boson.

1.2   Quantum ChromoDynamics (QCD)

Quantum Chromodynamics (QCD) describes the strong interaction in analogy with Quantum Electrodynamics (QED), the quantized field theory of electromagnetic force. In QED, electromagnetic interactions between electrically charged particles are described through the emission and absorption of the corresponding field mediators - photons; similarly, the QCD predicts the existence of mediators called gluons, which transmit the strong force between particles with the so-called color charge. Quantum Chromodynamics is a non-Abelian gauge theory based on the $SU(3)$ symmetry group in the three-dimensional space of color charges, which are conventionally referred to as Red, Green and Blue charges. The $SU(3)$ group theory is known to have 8 generators, whose physical counterparts are the gluons. The difference between QED and QCD is the fact that, in the first case, the force carriers - the photons, do not possess electric charge, whereas in the second case, the gluons do possess a colour charge and can therefore interact via the strong force. The strong force field mediators interact obeying different properties compared to the processes described by QED. Figure 1.2 describes the vertices of the fundamental interaction of quantum chromodynamics.
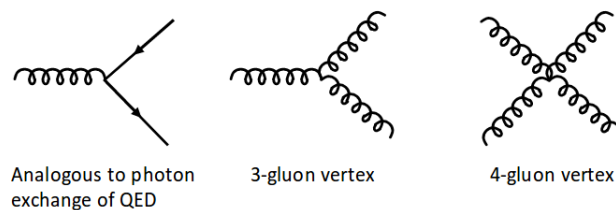

Figure 1.2: Basic interaction vertices of the QCD. From left to right: quark-quark gluon interaction, three gluon interaction, four gluon interaction.

1.2.1 Confinement and asymptotic freedom

In mathematical terms, each interaction vertex is characterized by a so called coupling constant, i.e. a dimensionless quantity that defines the intensity of the interaction on a given energy scale. In high energy scattering processes between leptons and nucleons, we can observe weakly bound quarks that behave like free particles. On the other hand, the theories on quantized fields show that the strong interaction coupling constant, conventionally labeled with α_s (or g_s) strongly depends on the energy involved and consequently on the transferred momentum q^2, so that as the momentum increases, the coupling constant tends asymptotically to 0. This leads to a phenomenon known as asymptotic freedom. In other words, at high energies or at small distances the intensity of the strong interaction drastically decreases, which is why the quarks and the gluons forming the bound systems (hadrons) behave as free particles. For low momentum values, on the other hand, the coupling constant grows rapidly. This implies that at low energies or at great distances the intensity of the strong interaction increases, leading to the opposite phenomenon - known as confinement - which is the reason why quarks in nature are found only within bound states.

1.3 Quark-Gluon Plasma (QGP)

As stated in the previous paragraph, at low values of temperature and baryonic density, QCD is dominated by the confinement phenomenon. As the temperature T and the energy density ρ increase, however, the coupling constant decreases, possibly leading to a phase transition from hadronic state (gas consisting of bound states of quarks and gluons) to a deconfined state governed by asymptotic freedom. In other words, at precise values of temperature and energy density, a transition occurs from the hadronic state to a system modeled as a fluid of weakly interacting quarks and gluons. This is the Quark-Gluon Plasma (QGP).

1.4 Phase transition in QCD: the Quark-Gluon Plasma (QGP)

In figure 1.3 we can observe the QCD phase diagram as a function of temperature T and bariochemical potential $\mu_B = \partial E / \partial N_B$ (which defines the amount of energy that needs to be supplied to the system in order to increase its baryonic number by a unit). As we can see, ordinary nuclear matter is formed at low T and μ_B values (hadronic phase) and as the energy increases we find the transition curves. The representation of these curves give us an idea of the system evolution, as the boundaries of the various phases of the QCD are still not well known. However, the transition curve of the QGP region is qualitatively appreciable, and it is possible to observe the existence of a further region which is defined by color charge superconductivity for low T and high of μ_B values. At the present state of research, it is estimated that the critical transition temperature from the hadronic to the plasma phase is $T_c = 0.16$ - 0.19 GeV. This estimate is however still object of debate within the scientific community.
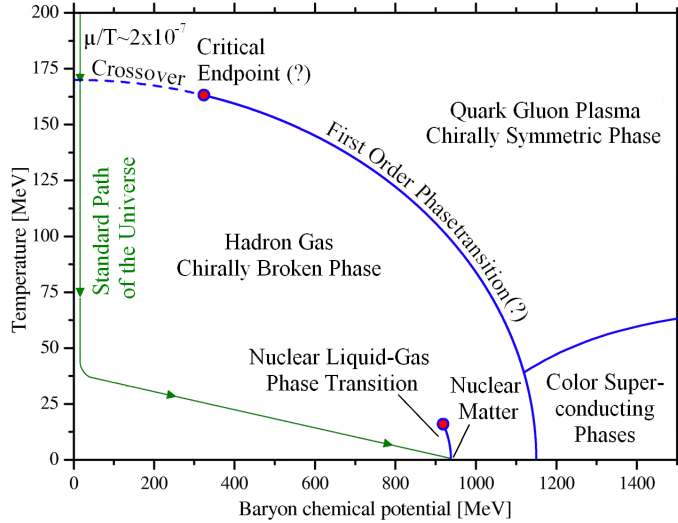
Figure 1.3: Phase transition graph for QCD.

1.5   Heavy-Ion collisions

When a collision between ultrarelativistic heavy ions occurs, the temperature and energy conditions necessary for QGP production are reached. Given the ultrarelativistic speed of the particles involved in the impact, we therefore take into account the Lorentz contraction as far as the beam propagation direction is concerned. We can think of the two nuclei that collide as two thin disks of radius $2R_A \simeq 2A^{1/2}$ fm, where A is the number of nucleons. The greater the centrality of the collision, the greater the likelihood of creating suitable conditions for the formation of the QGP. When the collision is not central, only a part of the nucleons is involved, while the others, called "spectators", continue along the beam direction basically unperturbed. The trajectories of the involved particles can described in terms of a kinematic variable called rapidity, defined as:

$$y = \frac{1}{2}\ln\left(\frac{E + p_L}{E - p_L}\right) = tanh^{-1}\left(\frac{p_L}{E}\right) \tag{1.1}$$

where E is the energy and p_L is the component of the momentum along the direction of the beam. This translates, in the ultrarelative limits, into another quantity called pseudorapidity:

$$\eta = \frac{1}{2}\ln\left(\frac{p + p_L}{p - p_L}\right) = -\ln\left(tan\frac{\theta}{2}\right) \tag{1.2}$$

where θ is the angle between the momentum and the direction of the beam.

1.5.1 Evolution of the QGP

The QGP is formed only in certain temperature and energy density conditions. If they are not reached, the system starts to evolve hydrodynamically via a preadronic phase, in which the deconfination does not take place [2][3]. In the first stages of the collision, the so called pre-equilibrium phase takes place, during which the production of particles with high transverse momentum ($p_T >> 1$ GeV/c) and the emission of direct, real or virtual photons occur. Virtual photons manifest in lepton-antilepton pairs ($e^+ e^-$ or $\mu^+ \mu^-$). Unlike what happens in proton-proton collisions, when dealing with heavy ions, the products of the collision cannot leave the area in which they have occurred, so they continue to collide and create a cloud of interacting particles which, when thermalizing with a sufficiently high energy density, forms the QGP. The system that is created is in thermal equilibrium, and therefore starts expanding under its own pressure and cools down. When the system returns to a critical density, it starts a quark and gluon hadronization process. The formation of hadrons can occur by fragmentation of a high momentum parton, or by coalescence, which is the fusion of low momentum hadrons. These processes continue until the energy becomes insufficient to allow inelastic collisions, reaching a state in which the relative abundances of chemical species are fixed, which is called chemical freeze-out [4]. The interactions, now due only to elastic collisions, stop when the distances between the hadrons become greater than the radius of strong interactions, forming the thermal freeze-out. The process described is represented in figure 1.4.
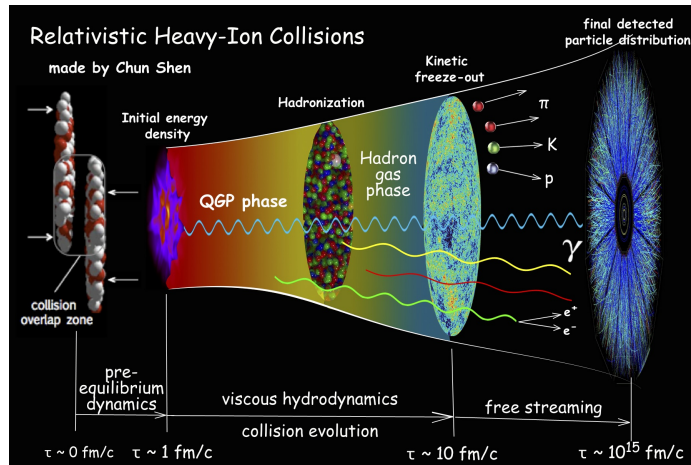

Figure 1.4: Representation of a collision between ultrarelativistic heavy ions and the QGP process of formation and evolution.

1.6 Experimental evidences of the QGP

The QGP is a difficult state of matter to manage in a laboratory, as not only it happens under particular physical conditions, but it is also characterized by a very short average lifetime. The study of this phase is therefore based on indirect observations: hard probes (signals produced in the early stages of collisions by interactions with partons with a high transverse momentum), or soft probes (signals produced in phases following the collisions and linked to interactions with low momentum partons). In the next paragraphs some of the experimental evidence supporting the existence of QGP the will be discussed.

1.6.1 Strangeness Enhancement

The enhancement in strangeness production in heavy-ion collisions was one of the first proposed signatures of the QGP formation [5]. Strange quark and antiquark counterparts are not present in the initial lead ions and are therefore a new product of the process. In the normal processes of collisions between hadrons, the creation of states containing strange quarks is suppressed due the lower mass of the up and down quarks. This suppression increases as the contained strangeness increases. In a QCD phase, on the other hand, the production of the s quark is abundant because, due to the partial restoration of the chiral symmetry, their mass is equal to $m_s \sim 150$ MeV/c^2 ("bare" mass, i.e. without dynamic effects). Also, the Pauli exclusion principle limits the number of u and d quarks present in the plasma due to the saturation of accessible states. The very high density of gluons within the Quark-Gluon Plasma facilitates the production of $s\bar{s}$ pairs via the gluonic fusion process. Only 10-15% is due to the annihilation between quarks and antiquarks, the remaining interactions between the gluons that are free due to the QGP deconfinement. This process is called thermal production, as it can be compared to a gas of partons in thermal equilibrium. In this deconfined state the increase of strangeness causes a greater probability, during the chemical freeze-out, of the formation of hadrons containing one or more strange quarks, such as Ω^+ ($\bar{s}\bar{s}\bar{s}$), Λ^0 (uds), Ξ^0 (uss), Ξ^- (dss), Ω^- (sss). As can be seen in figure 1.5, the ratio increases when the number of nucleons participating in the collision increase, i.e. with the growth of centrality.
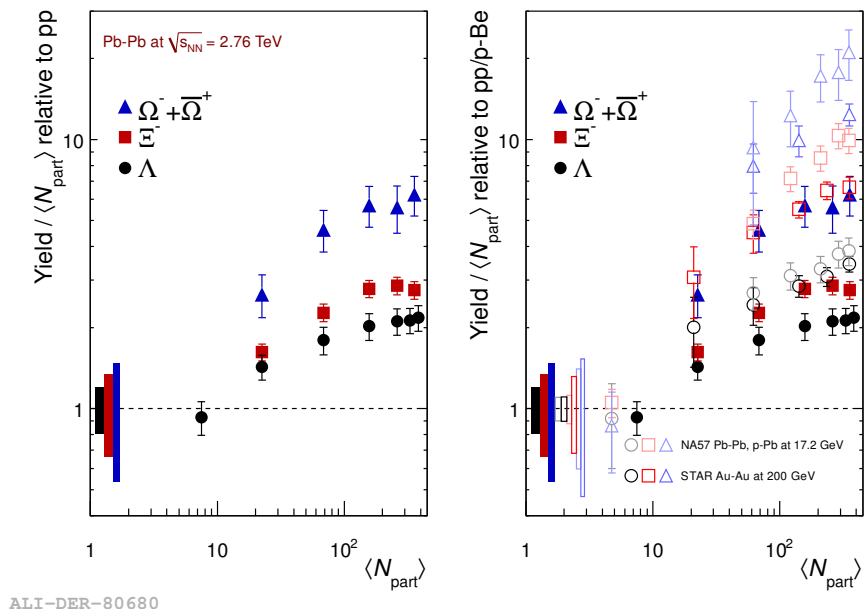

Figure 1.5: Increase in the rate of hyperons production in ALICE in Pb-Pb collisions at $\sqrt{s_{NN}} = 2.76$ TeV, which represent the increasing of strangeness according to the average number of participants (left) and comparison with the data taken at SPS and RHIC at lower energies (right).

9

1.6.2 J/Ψ suppression

The set of bound heavy quark states such as charmonium ($c\bar{c}$) and bottonium ($b\bar{b}$) is called Quarkonia. In a deconfined, high temperature medium such as the Quark-Gluon Plasma, we expect the production of states to be suppressed compared to pp collisions, as seen in figure 1.6 where the nuclear modification factor R_{AA}, defined as the J/ψ cross section in Pb-Pb collisions divided by the cross section in pp collisions scaled by the lead mass number A = 208, is shown as a function of the number of participating nucleons. This is because of the colour screening of the force that holds these quarks bound. Strongly bound states such as J/ψ and Υ dissipate at higher temperatures than more weakly bound states. The effect of the colour charge screening that occurs within the dense and hot nuclear material, divides the J/ψ into its constituents c and $\bar{c}$; as long as the screening radius is greater than the binding radius, the quarks are held together by the strong force. When the dimensions of the bound state become greater than the screening radius, the deconfinement occurs: the components get separated and when the hadronization takes place, they combine with light quarks to form mesons. The level of J/ψ suppression is proportional to the temperature and the colour charge density.
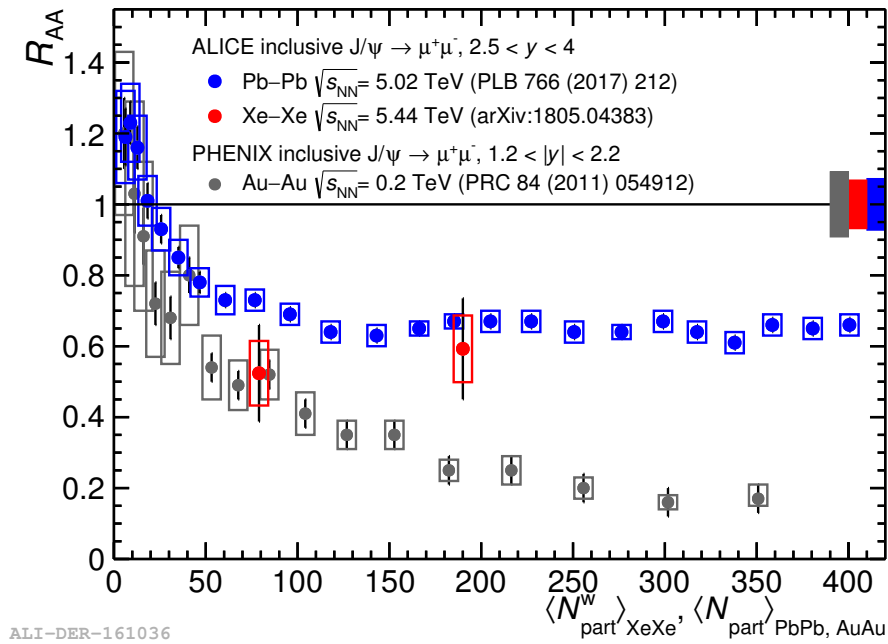

Figure 1.6: Measurements in ALICE for Pb-Pb collision at $\sqrt{s_{NN}} = 5.02$ TeV and for Xe-Xe collisions at $\sqrt{s_{NN}} = 5.44$ TeV compared to RHIC measurements for Au-Au collisions at $\sqrt{s_{NN}} = 200$.

1.6.3 Jet quenching

A jet is a collimated beam of products from the hadronization process. The Jet Quenching phenomenon [6] consists of an energy dissipation due to the interaction of the emitted partons with the medium within which they propagate, namely the QGP. The energy loss is basically due to a braking gluonic radiation (gluonic Bremsstrahlung effect). The dissipative effect depends on the distance traveled inside the propagating medium and translates into an overall loss of transverse momentum. The phenomenon is observed most frequently in the case of central collisions. The suppression of high transverse momentum particles is quantifiable through the nuclear modification factor R_{AA}. In general, in the absence of nuclear modification factors on hard scattering processes, we have $R_{AA} = 1$. If we observe deviations from this value, it indicates the presence of modification effects which are an indicator of the presence of QGP. In particular, for $R_{AA} > 1$ we have amplification, while for $R_{AA} < 1$ we have suppression regarding the yielded particles. The results of the ALICE measurements in Pb-Pb collision events at $\sqrt{s_{NN}} = 2.76$ TeV, visible in figure 1.7, show a general suppression phenomenon for all the centrality classes with minimum a $p_T = 6$ - 7 GeV with respects to an overlap of binary pp collisions. Furthermore, it is easily noticeable that the central collisions depend more strongly on the transverse momentum and are subject to larger suppression, presumably due to the fact that the particles dissipate more energy, as they spread from the central region, having to cross greater distances within the QGP.
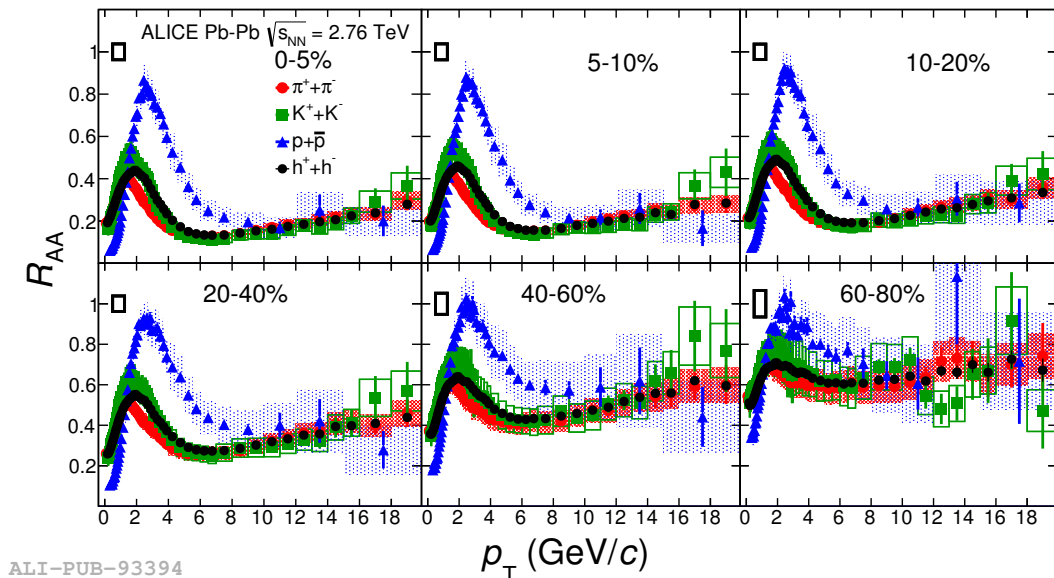

Figure 1.7: Nuclear modification factor for different types of particles as a function of the transverse momentum. The results of the Pb-Pb collision events in ALICE at $\sqrt{s_{NN}} = 2.76$ TeV for different centrality intervals [7] are shown.

1.6.4 Direct Photons

Direct photons, defined as photons which haven't been produced by a hadron decay, are an important tool for studying the evolution of the QGP. Unlike hadrons, direct photons are produced during all phases of the collision. Due to the fact that they lack strong color charge, they do not interact with the plasma constituents, providing direct information on the conditions in which they were created, such as temperature, collective motions and system space-time evolution. Different intervals of p_T correspond to photons emitted at different times; at high p_T (> 5 GeV) the spectrum is dominated by prompt photons, created by high momentum transferred collisions (hard probes), while for lower momenta the spectrum is dominated by thermal photons produced in the partonic and hadronic phase. This type of measurement ends up being complicated because of the large background caused especially by the decay of the π^0 and η mesons, and the separation of the different components in the inclusive spectrum. Figure 1.8 shows the direct photon spectrum measured in ALICE in Pb-Pb central collisions at $\sqrt{s_{NN}} = 2.76$ TeV. Comparing the measured spectra in proton-proton collisions with those in heavy ion collisions, we can observe a greater number of photons produced at low transverse momenta in the latter. With an exponential fit of the spectrum in the 0-20% centrality range, we get a temperature of about 297 MeV, which corresponds to the temperature of the photon source mediated along its whole temporal evolution. This value indicates an initial temperature far above of the critical temperature at which the QGP is formed, equal to about 150-160 MeV.
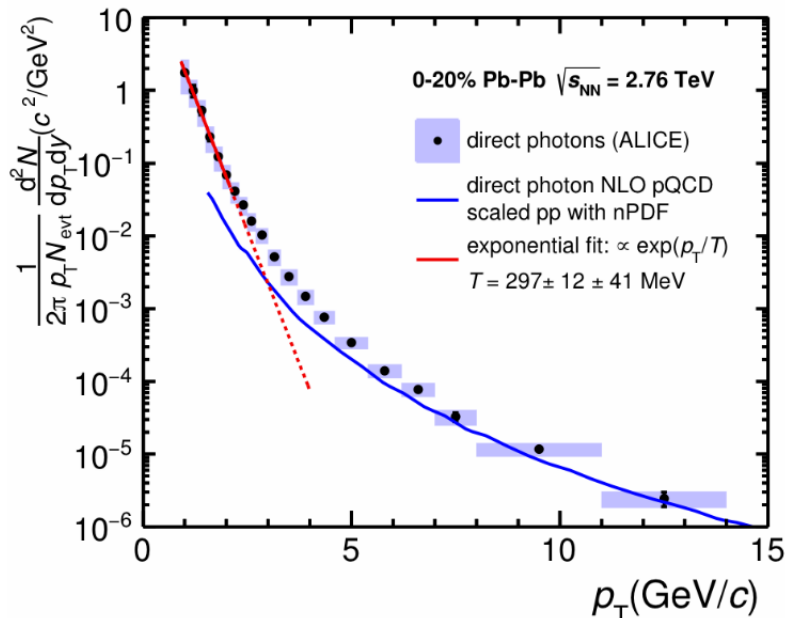

Figure 1.8: Direct photon spectrum measured in ALICE in Pb-Pb central collisions at $\sqrt{s_{NN}} = 2.76$ TeV.

Chapter 2

The ALICE detector at the LHC

2.1 The Large Hadron Collider (LHC)

The Large Hadron Collider (LHC) at CERN is the world's largest and most powerful particle accelerator; it is a circular hadron collider consisting of a 27-kilometer ring of superconducting magnets. Inside the accelerator, two high-energy beams travel at close to the speed of light before they are made to collide at four interaction points, corresponding to the position of four experiments: ALICE, ATLAS, CMS and LHCb, as shown in figure 2.1. The beams travel in opposite directions in separate beams pipe in ultra-high vacuum conditions and are guided by a system of superconducting magnets (including 1232 dipole magnets 15 meters long to keep the beams on their circular path and 392 quadrupoles magnets which focus the beams) cooled down at a operating temperature of 1.9K, colder than the outer space.
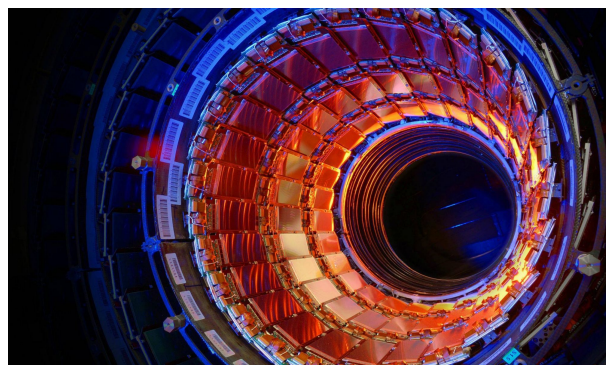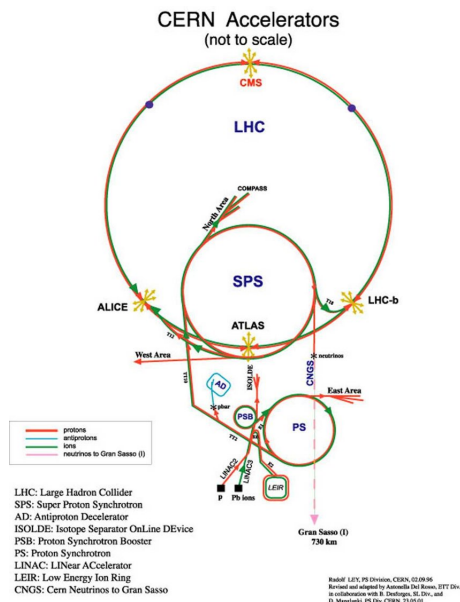

Figure 2.1: Images of the LHC experiment.

2.2 The ALICE experiment

ALICE (A Large Ion Collider Experiment) [8] represented in figure 2.2 is the heavy-ion detector at the Large Hadron Collider (LHC) ring. It is designed to study the physics of strongly interacting matter at extreme energy densities, where the quark-gluon plasma is formed. Such conditions are believed to have existed a few microseconds after the Big Bang, before quarks and gluons bonded to form hadrons. All ordinary matter in today's universe is made up of atoms. Each atom contains a nucleus made of protons and neutrons, surrounded by a cloud of electrons. Protons and neutrons are made of quarks which are bound together by other particles called gluons. No free quarks have ever been observed: the quarks, as well as the gluons, seem to be bound permanently together and confined inside composite particles, such as protons and neutrons. This is known as confinement. Collisions in the LHC generate temperatures 10000 times hotter than the centre of the Sun. Each year the LHC provides collisions between lead ions, recreating similar conditions in the laboratory to those just after the Big Bang. Under these extreme conditions, protons and neutrons melt, freeing the quarks from their bonds with the gluons. This is quark-gluon plasma. The existence of such a phase and its properties are a key issue in the theory of quantum chromodynamics (QCD) for understanding the confinement, and for a physics problem called chiral-symmetry restoration. The ALICE collaboration studies the quark-gluon plasma as it expands and cools, observing how it progressively gives birth to the particles that constitute the matter of our universe today. The ALICE Collaboration uses the 10000 tonne ALICE detector - which is 26 m long, 16 m high, and 16 m wide - to study quark-gluon plasma. The detector lies in a vast cavern 56 m underground close to the village of St Genis-Pouilly in France, receiving collisions from the LHC. The Collaboration counts more than 1500 scientist from over 100 institutes in 37 countries across the world.
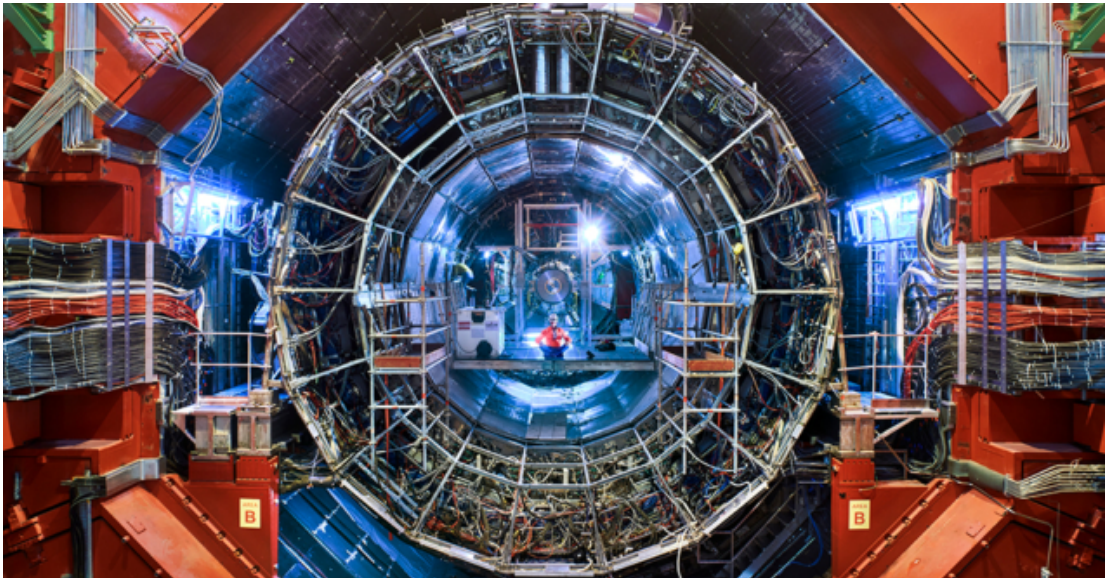

Figure 2.2: Photo of the ALICE experiment.

The experiment consists of 18 different detector systems, shown in figure 2.3, each with its own specific technology choice and design constraints, driven both by the physics requirements and the experimental conditions.

THE ALICE DETECTOR

a. ITS SPD (Pixel)
b. ITS SDD (Drift)
c. ITS SSD (Strip)
d. V0 and T0
e. FMD

1. ITS
2. FMD, T0, V0
3. TPC
4. TRD
5. TOF
6. HMPID
7. EMCal
8. DCal
9. PHOS, CPV
10. L3 Magnet
11. Absorber
12. Muon Tracker
13. Muon Wall
14. Muon Trigger
15. Dipole Magnet
16. PMD
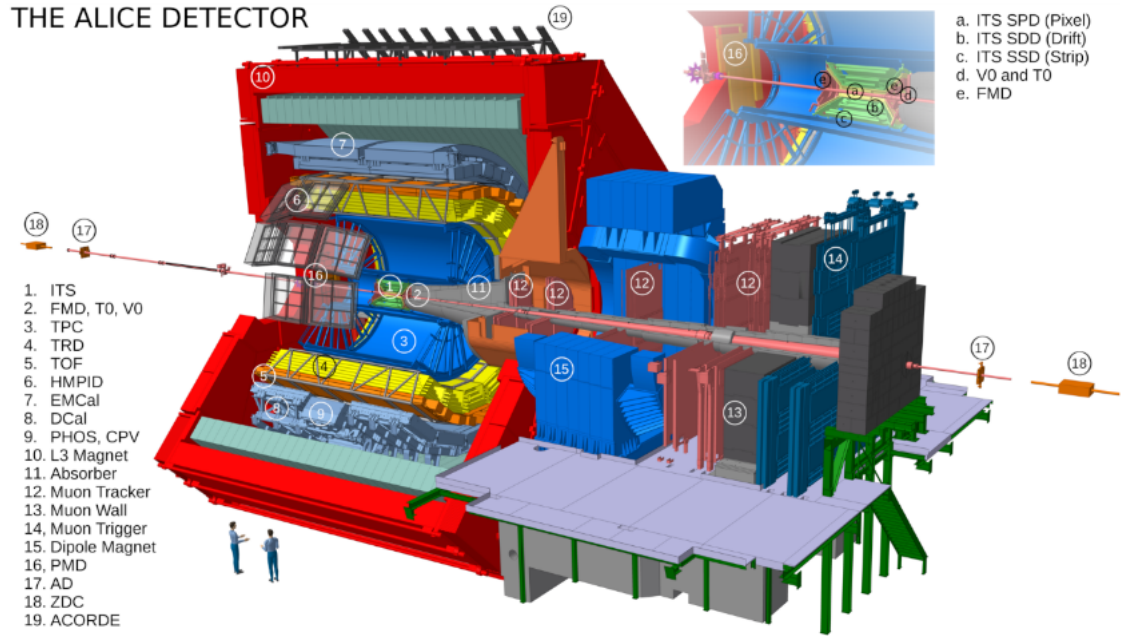17. AD
18. ZDC
19. ACORDE

Figure 2.3: Schematic representation of the structure of the ALICE detector.

- The *tracking detectors* have the task of reconstructing the vertices of interaction and decay and the trajectories of charged particles in the magnetic field and allow to obtain accurate position and momentum measurements. These are the ITS (Inner Tracking System), the TPC (Time Projection Chamber) and the TRD (Transition Radiation Detector).

- The *Particle IDentification detectors* allow to associate an identity to the reconstructed trajectories by the tracking detectors. These include the TOF (Time-Of-Flight) and HMPID (High Momentum Particle IDentification).

- The electromagnetic PHOS (Photon Spectrometer), EMCAL (Electro-Magnetic Calorimeter) and DCAL (Di-jet Calorimeter) *calorimeters* allow to measure the energy of charged and neutral particles.

- The *muon spectrometer* formed by MCH (Muon Chamber) and MTR (Muon Trigger), which cover a region of forward rapidity ($2.5 < \eta < 4$) and is dedicated to the study of heavy-quark resonances.

- The *forward and trigger detectors* which are the FMD (Forward Multiplicity Detector), the PMD (Photon Multiplicity Detector), AD (ALICE Diffractive), the ZDC (Zero Degree Calorimeter), V0 and T0.

- The *cosmic ray trigger detector* ACORDE (A Cosmic Ray Detector).

In the following sections, we have a brief description of the main tracking and PID ALICE detectors.

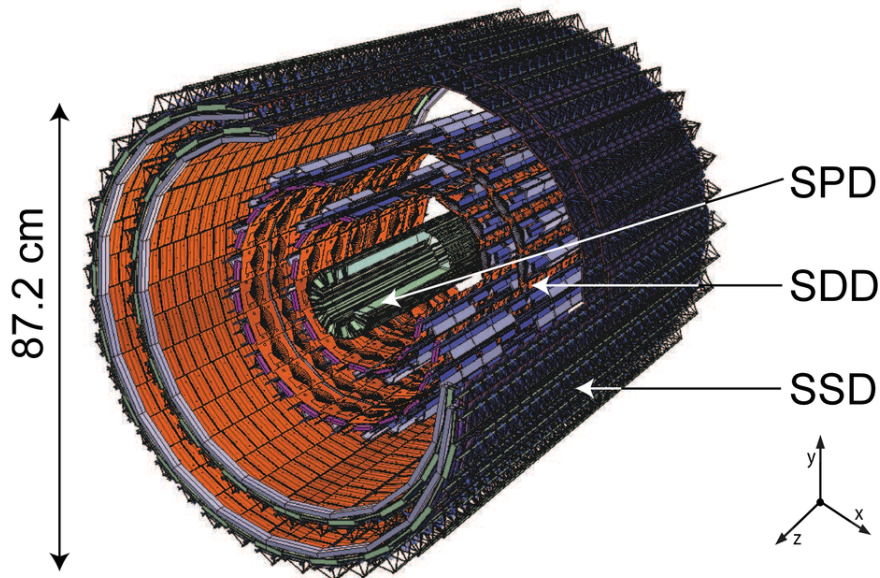## 2.2.1   Inner Tracking System (ITS)

Figure 2.4: Schematic representation of the ALICE ITS.

The first detector that the particles encounter after their collision is the ITS, which is the innermost layer of the ALICE structure (figure 2.4). It covers a pseudorapidity range of $|\eta| < 0.9$ over the entire azimuth angle and its radius extends from 3.9 cm to 43 cm. It is formed by six concentric layers of silicon detectors. The two Silicon Pixel Detector (SPD) layers are designed for dealing with the large density of charged particles produced in the ion-ion collisions, while more externally, where the density of particles decreases, there are two 2-dimensional detectors, which are the Silicon Drift Detector (SDD) and the Silicon Strip Detector (SSD). The main objectives of the ITS are the localization of the primary vertices, with a resolution better than 75 μm for tracks with $p_T > 1$ GeV/c and the reconstruction of the secondary vertices from the decay of the B and D mesons and hyperons. It also has the task of improving the momentum measurement and the angular resolution of the particles reconstructed by the TPC, also tracking charged particles with $p_T < 200$ MeV/c which fail to get to the outermost detectors.
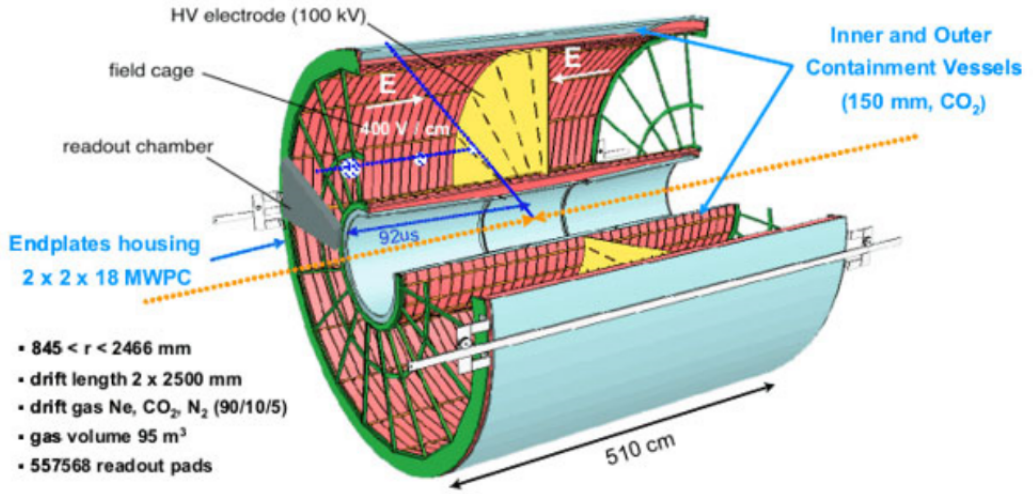
2.2.2 Time Projection Chamber (TPC)

Figure 2.5: Schematic representation of the ALICE TPC.

The TPC is the main tracking detector, optimized for particle identification in a very wide range of momenta, up to a value equal to 10 GeV/c, with pseudorapidity coverage of $|\eta| < 0.9$, on the whole azimuth angle. The identification of the particles with low momenta occurs through the measurement of the loss of ionization energy, $-\frac{dE}{dx}$ described by the Bethe-Bloch relativistic formula, applicable to charged particles traveling at high speeds [9]. The TPC also has the task of reconstructing the primary vertices of charged particles starting from the outermost regions, where the track density is lower, up to the innermost ones in which they are so abundant as to have numerous overlays. The detector (figure 2.5) has a cylindrical shape with an internal radius of 85 cm and external radius of 250 cm and a length of about 5 meters, covering a volume of 88 m^3, filled with a gas mixture composed of 90% neon and 10% carbon dioxyde which reduces multiple scattering effects [10].
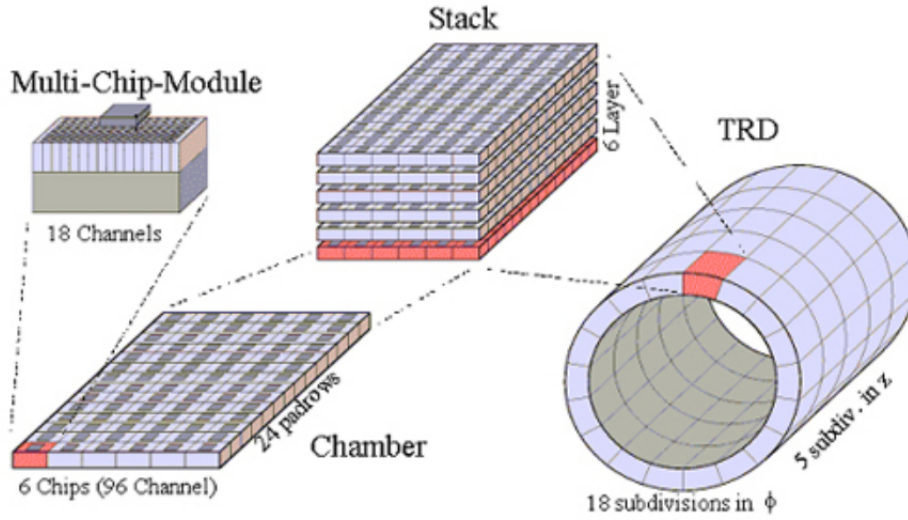
2.2.3 Transition Radiation Detector (TRD)

Figure 2.6: Schematic representation of the ALICE TRD.

Outside the TPC is the TRD detector (figure 2.6) that extends from a radius of 2.9 m to 3.7 m with a length of 7 m. It is made of an inhomogeneous material called radiator and is divided in 522 readout chambers arranged on 6 levels, each filled with a gas mixture formed of 85% Xe and 15% of CO_2 and divided by a cathode grid into 3 drift and one amplification region, in which we have an anode. The main task of this detector is the identification of electrons and positrons with momenta above 1 GeV/c. The identification is possible by exploiting the transition radiation that the relativistic charged particles and in particular the electrons emit when they pass from one material to another with different dielectric constants. Figure 2.7 shows the shape of the electrical signal induced by a pion and an electron in a readout chamber; the presence of a long-time peak due to photons emitted by transition radiation allows to identify electrons.
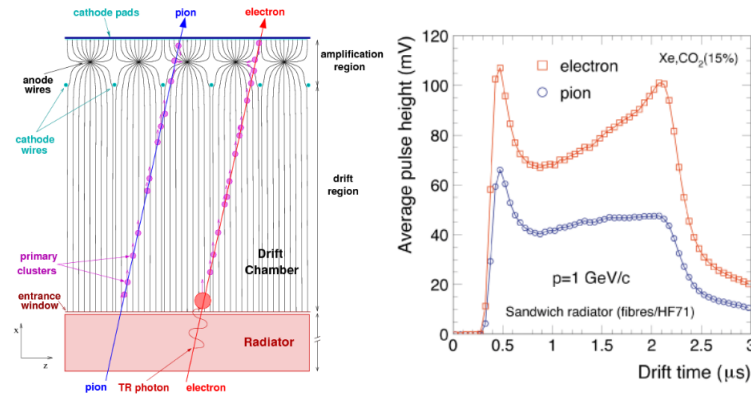

Figure 2.7: On the left there is the schematization of a chamber of the TRD, whereas on the right, the graph shows the signal induced by a pion and an electron as a function of the drift time; the second long-time peak on the red curve, due to the emitted photon, proves that this curve belongs to an electron.
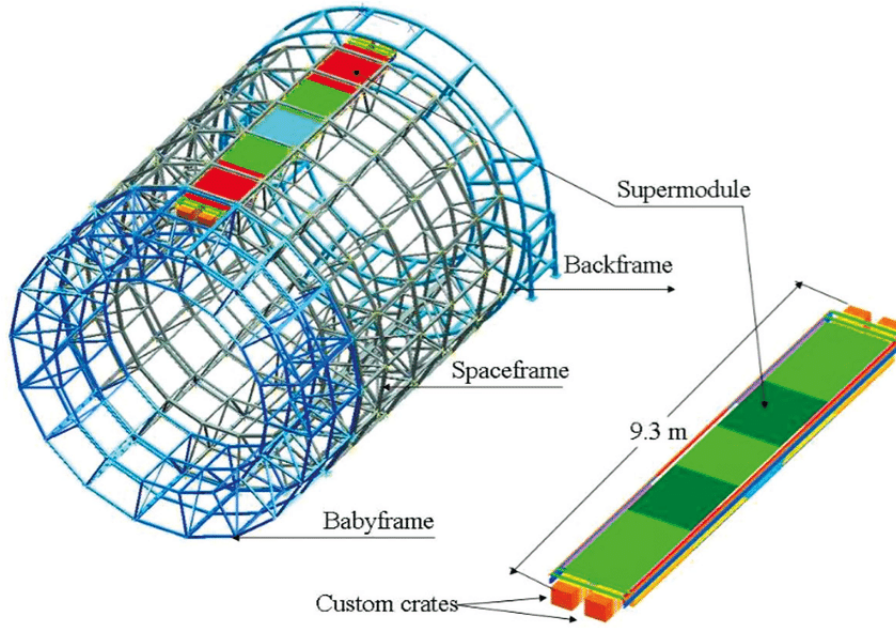
18

2.2.4 Time-Of-Flight (TOF)

Figure 2.8: A schematic layout of the TOF system.

Charged particles in the intermediate momentum range are identified in ALICE by the Time-Of-Flight detector (figure 2.8). The time measurement with the TOF, in conjunction with the momentum and track length measured by the tracking detectors, is used to calculate the particle masses. A time resolution of 100 ps will provide $3\sigma \pi/K$ separation up to 2.5 GeV/c and K/p separation up to 4 GeV/c. It is located 3.7 m away from the central axis and has a cylindrical structure covering the central region of pseudorapidity $|\eta| < 0.9$ on the entire azimuth angle ϕ, for a total area of 140 m^2. The apparatus has a modular structure, made up of 18 sectors in ϕ and 5 segments along the axial coordinate. Each one of the 90 modules contains a variable number of Multigap Resistive Plate chamber strips (MRPC). They are divided into two regions, the internal one containing a gaseous mixture of tetrafluroethane ($C_2H_2F_4$), isobutane (C_4H_{10}) and hexasulfur fluoride (SF_6) with a 90:5:5 ratio, where the MRPC are located; and an external one where we find the front-end electronics which are connected through wires of various lengths to the readout modules.

Chapter 3

Λ_c Reconstruction with Artificial Neural Networks

3.1 Introduction

The study of heavy quarks is one of the fundamental tools to investigate the properties of Quark-Gluon Plasma created in ultrarelativistic heavy-ion collisions. Due to their high mass, charm quarks are created in the very early stages of the collision and, propagating inside the medium, they can interact with its constituents during the entire evolution of the system, providing a direct measure of its own property. The production of charm baryons is of particular interest because it is sensitive to the processes of hadronization in the medium. The charm baryon Λ_c, whose properties are illustrated in table 3.1, was reconstructed in ALICE through two hadronic decay channels and the semileptonic channel; in particular, in this thesis, we analise the $\Lambda_c^+ \to p K_S^0$ decay. In the analysis of this decay we have encountered two particular challenges. One is due to the short average life (at rest) of Λ_c; in fact, on average, before decaying it covers a distanceof about 60 μm, less than the precision of the ALICE microvertex detector (equal to about 100 μm) thus making it impossible to distinguish between primary and secondary vertices. The second is due to the low signal over background ratio. Multivariate analysis techniques have proven to be very useful in improving the decay reconstructions, thanks to the advantage of considering properties of multiple events simultaneously, thus exploiting most of the variable information through machine learning techniques. A software implementation of multivarate analysis techniques is already provided inside of the TMVA package distributed within the ROOT analysis framework.

Content	Mass (MeV/c^2)	Mean lifetime ($10^{-15}s$)
udc	2286.46 ± 0.14	200 ± 6

Table 3.1: Main properties of the charm baryon Λ_c.

3.2 TMVA

The Toolkit for Multivariate Data Analysis (TMVA) [11] is a ROOT-integrated package that provides a machine learning environment for the processing and evaluation of multivariate classification and regression techniques targeting applications in high-energy physics. All multivariate techniques in TMVA belong to the family of "supervised learning" algorithms. Among the different classifiers, the artificial neural network with multi-layer perceptron (MLP) has been chosen for the present thesis.

3.3 Neural Networks MLP

Neural networks are computing systems based on an analogy with the functioning of the human brain. The neurons, which correspond to the nodes, are modeled as basic functions that are activated or not depending on whether a threshold level is reached. These functions are joined through a weighted linear combination of the input variables. The resulting function is sent to the next level through links, corresponding to the synapses, whose thickness is proportional to the weight associated to them. The network can be formed, in addition to input and output levels, also by intermediate hidden levels: the more numerous these are, the more precise the output will be. The MLPs are a particular type of neural networks in which the output of each node of a leve is used only as an input of one or more nodes of the next level, but cannot return to the previous ones creating a loop. In the input level we also find an additional node, the bias node, always set to 1, necessary if all the input variables are 0; in this case, otherwise, the value passed to the next level, calculated as the weighted average of their values would always be equal to 0. The configuration of the neural networks we used is summarized in table 3.2. The activation function used is the hyperbolic tangent. It returns a weight between 1 and -1, respectively when there is a high or low input value. Its particularity is being a continuous function and therefore it allows outputs which are intermediate values of the maximum and minimum, a fundamental characteristic for the learning algorithm of multilevel neural networks, such as the one we used. In particular, the input layer contains N=12 neurons that correspond to the 11 variables of entrance and the bias, while hidden layers have been configured as to have N+5=17 neurons in the first level, N=16 in the second and so on, up to arriving at a single output neuron. For the training, 600 cycles were carried out, which were sufficient to have a final output that is very close to the one required.

Parametres	Values	Description
Neuron Type	tanh	Type of neuron function activation
VarTransform	N	Transformation of variables
NCycles	600	Numer of cycles used for training
Hidden Layers	N+5	Specification of architecture in hidden layers
Test Rate	5	Overtraining test performed at every age

Table 3.2: Configuration options for the MLP method.

The MLP algorithm needs a sample of training events, for which the desired output is known (signal or background candidates), to determine the mapping function that describes a decision boudary (classification). The learned mapping function is then applied to real data samples, in which the type of candidate is unknown.

3.3.1   Monte Carlo Simulations

The MLP algorithm was trained with a sample of simulated events, containing true Λ_c candidates and including a detailed description of the experimental apparatus and the detector response, for the signal candidates and with real candidates, sitting in the two side bands around the Λ_c invariant mass peak, taken by the ALICE experiment during the 2018 Pb-Pb data taking campaign for the background candidates. The training sample for signal-like candidates was taken from a simulation of PYTHIA6 [12] events containing charmed hadrons, embedded into an underlying Pb-Pb collision generated with HIJING [13] to obtain a better description of the multiplicity distribution observed in the data; the generated particles were then transported through the ALICE detector by using GEANT3 [14]. The presence of at least one Λ_c decaying via the hadronic decay channel under consideration in each simulated event was required in order to maximise the number of candidates.

3.3.2   BDT Input Variables

The machine learning method was run using 11 input variables:

1. **massK0S**

   V0 invariant mass reconstructed using the reconstructed tracks of the two daughters.

2. **impParBach**

   proton impact parameter, defined as the minimum distance between the reconstructed track of the proton and the position of the primary vertex.

3. **impParV0**

   impact parameter of the K_S^0 with respect to the primary vertex.

4. **ctK0S**

   cτ of the K_S^0, which is the distance between the primary vertex and that from which the two pions start, multiplied by the mass of the K_S^0 and divided by its momentum.

5. **cosPaK0S**

cosine of the pointing angle; i.e. the angle between the reconstructed direction of the K_S^0 (based on the momenta of the two pions) and the straight line joining the primary vertex and the decay vertex of the K_S^0.

6. **cosThetaStar**

cosine of the angle between the emission direction of the proton in the reference system in which the Λ_c is at rest and the direction of the Λ_c in the laboratory.

7. **signd0**

impact parameter of the proton with sign, defined in figure 3.1:
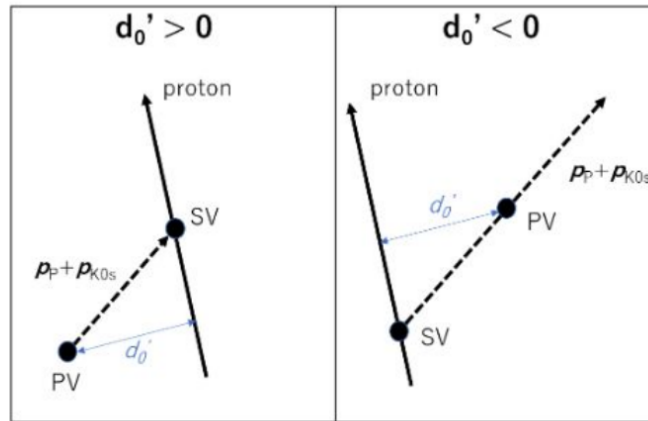
Figure 3.1: signd0 impact parameter.

The sign is defined as positive if the sum of the x-coordinate of the secondary vertex multiplied by the momentum of the Λ_c candidate along the x axis and the y-coordinate of the secondary vertex multiplied by the momentum of the Λ_c candidate along the y axis are greater than 0. The case with signd0>0 is much more compatible with a proton created by the decay of an Λ_c compared to the case with signd0<0, in which the proton appears to come from a point "before" the primary vertex.

8. **nSigmaTOFpr**

   Probability that the associated bachelor track is a proton, as calculated by the TOF detector. It is defined as the difference between the measured flight time from the TOF detector and the expected one in case the particle is actually a proton, divided by the resolution of the TOF detector(figure 3.2).
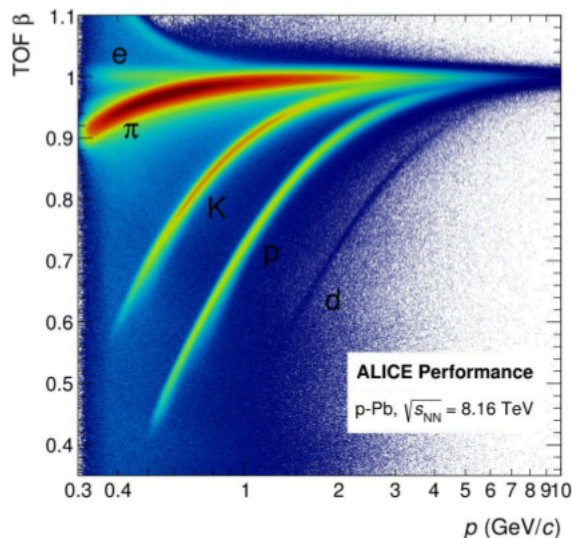

Figure 3.2: Beta measured by TOF as a function of the momentum. Different species (labelled) are clearly visible.

9. **nSigmaTPCpr, nSigmaTPCpi, nSigmaTPCka**

   Probability that the associated bachelor track is a proton, a pion or a kaon, respectively, as measured by the TPC detector, it is defined as the difference between the specific ionization in the TPC and the expected one in case the particle is actually a proton, a pion or a kaon, divided by the resolution of the TPD detector(figure 3.3).
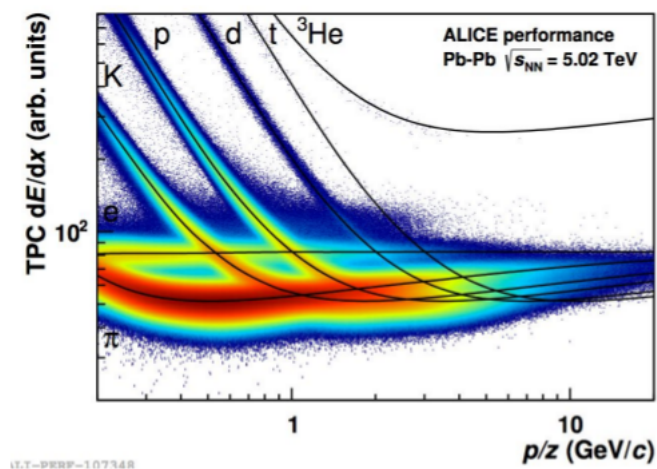

Figure 3.3: Specific energy loss in the TPC as a function of the momentum with superimposed Bethe-Bloch lines for various particle species (labelled).

We decided to analyse five intervals of transverse momentum : [3-4], [4-5], [5-6], [6-8], [8-10] GeV/c. The trainings were repeated independently on the different intervals. The distribution of the signal overlapping with the background for the 11 input variables for each interval can be observed from the graphs in the figures 3.4-3.8
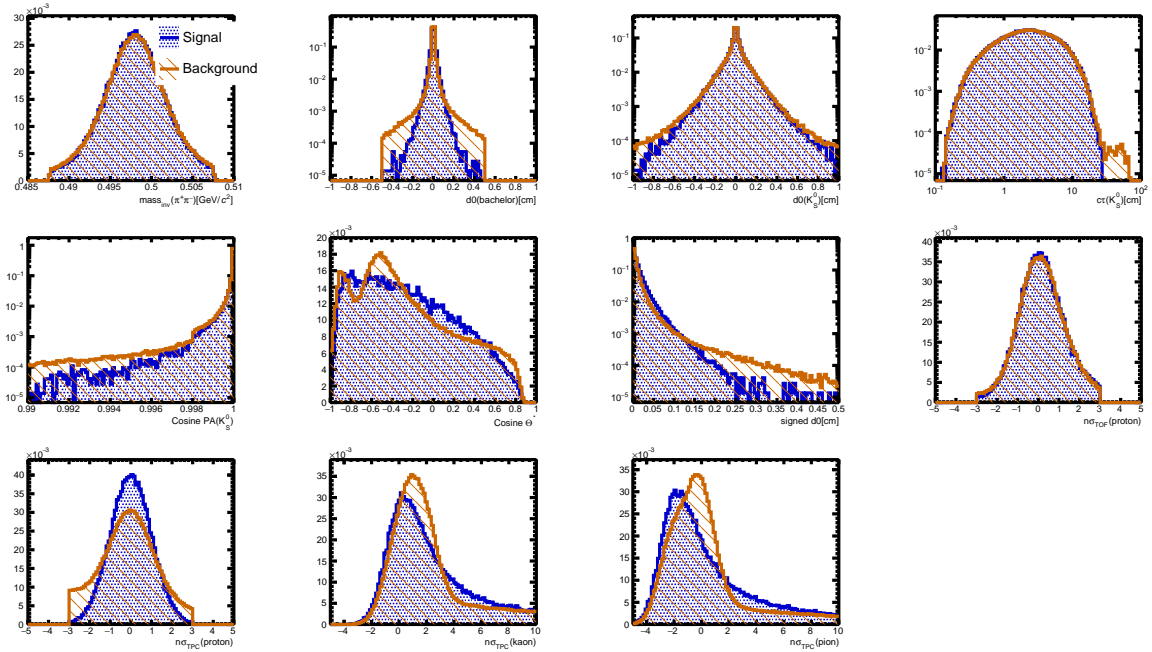

Figure 3.4: Input variable distributions for signal (blue-solid histogram) and background (red-hatched histogram) in the p_T interval [3-4] GeV/c.
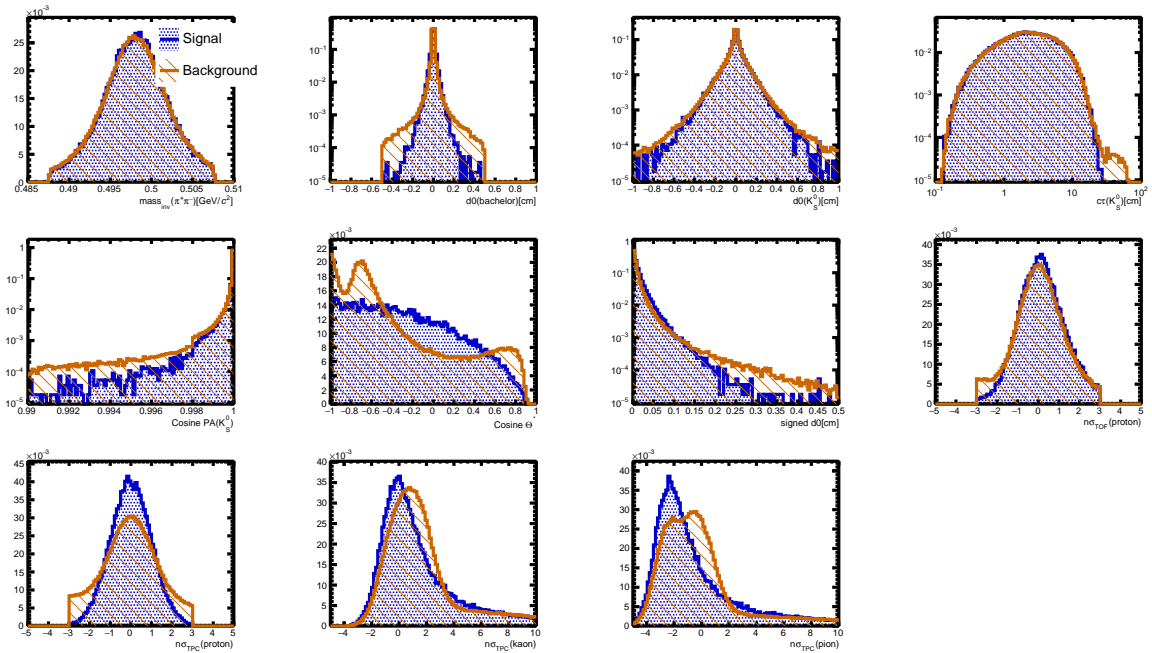

Figure 3.5: Input variable distributions for signal (blue-solid histogram) and background (red-hatched histogram) in the p_T interval [4-5] GeV/c.
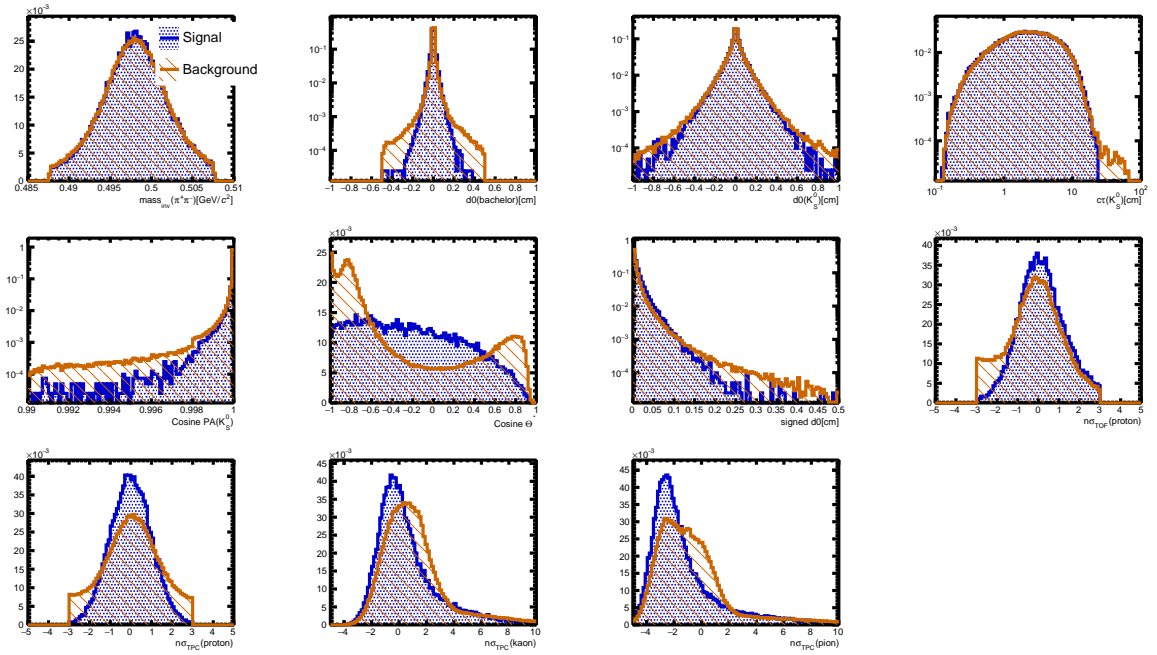
Figure 3.6: Input variable distributions for signal (blue-solid histogram) and background (red-hatched histogram) in the p_T interval [5-6] GeV/c.
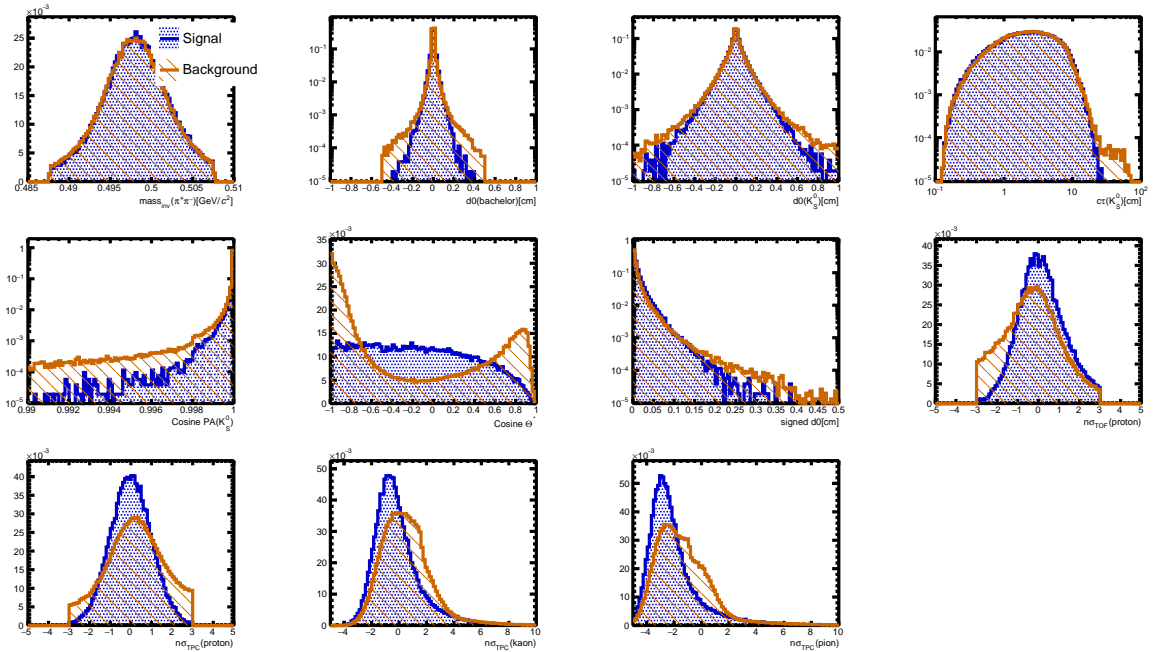

Figure 3.7: Input variable distributions for signal (blue-solid histogram) and background (red-hatched histogram) in the p_T interval [6-8] GeV/c.
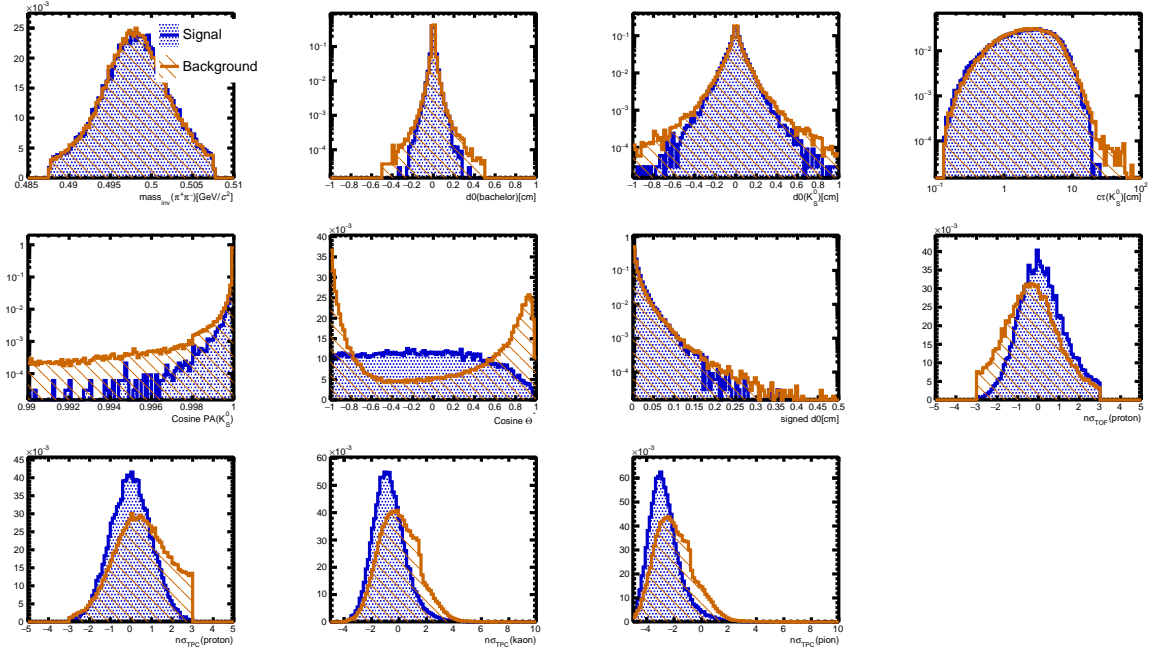
Figure 3.8: Input variable distributions for signal (blue-solid histogram) and background (red-hatched histogram) in the p_T interval [8-10] GeV/c.

It is useful to quantifiy the correlations between the input variables. Some classifiers underperform in presence of variable correlations. Moreover, correlated variables might unnecessarily increase the processing training time. The linear combination coefficients of the 11 input variables are calculated for every p_T interval to ensure they form a good set.

The correlation matrix regarding both the signal and background in the range [3-4] GeV/c is shown in figure 3.9 and is very similar in all the other intervals.
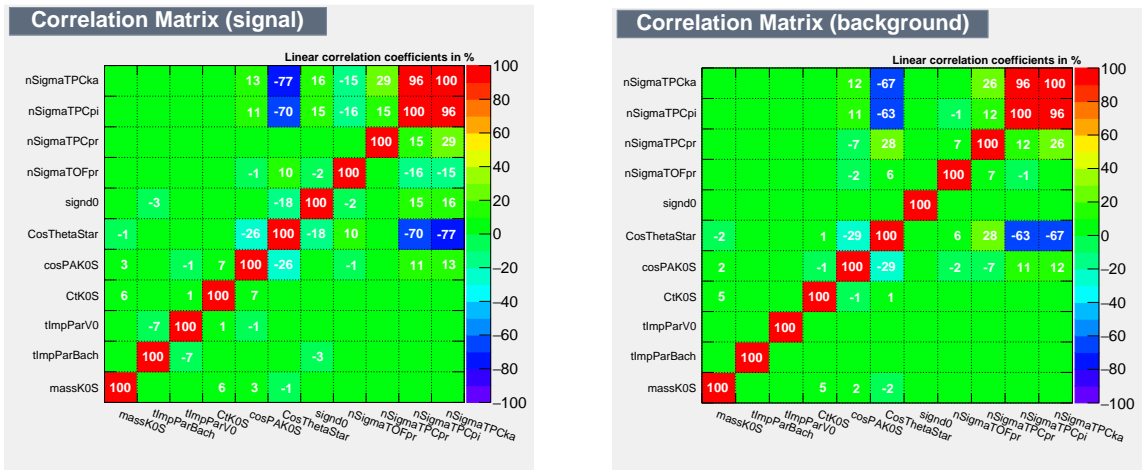

Figure 3.9: Linear correlation coefficients for the MLP input variables for the variables for the Λ_c signal candidates with transverse momentum in the [3-4] GeV/c range.

3.4   MLP Training

Before running the classification algorithm, the TMVA was configured in order to use both the signal and background samples for training and testing randomly; sampling them with an equal amount of events for the two processes. Comparing the performance results between training and test samples allows to assure the quality of the training process. The number of signal and background candidates are reported in table 3.3 (overall) and in table 3.4 (for each p_T interval).

	Signal	Background	Total Events
Number of Events	513957	6886298	7400255

Table 3.3: Sum of the training and testing events.

bin	Signal Events	Background Events
3-4	73314	500000
4-5	56728	500000
5-6	40648	383581
6-8	53067	305690
8-10	33220	103480

Table 3.4: Training events belonging to each interval of transverse momentum, for both signal and background.

3.5   MLP Outputs

The first output of the MLP classification is the comparison between the training and the testing of the classifier to verify that the results are not affected by overtraining. Overtraining occurs when a machine learning problem has too few degrees of freedom, because too many model parameterse of an algorithm were adjusted to too few data points. The comparing of the MLP response functions is reporetd in figure 3.10. When the classification is applied to the testing sample, the same output is obtained. This means that the specific choice of a certain sample to train the algorithm does not introduce any bias in the output.
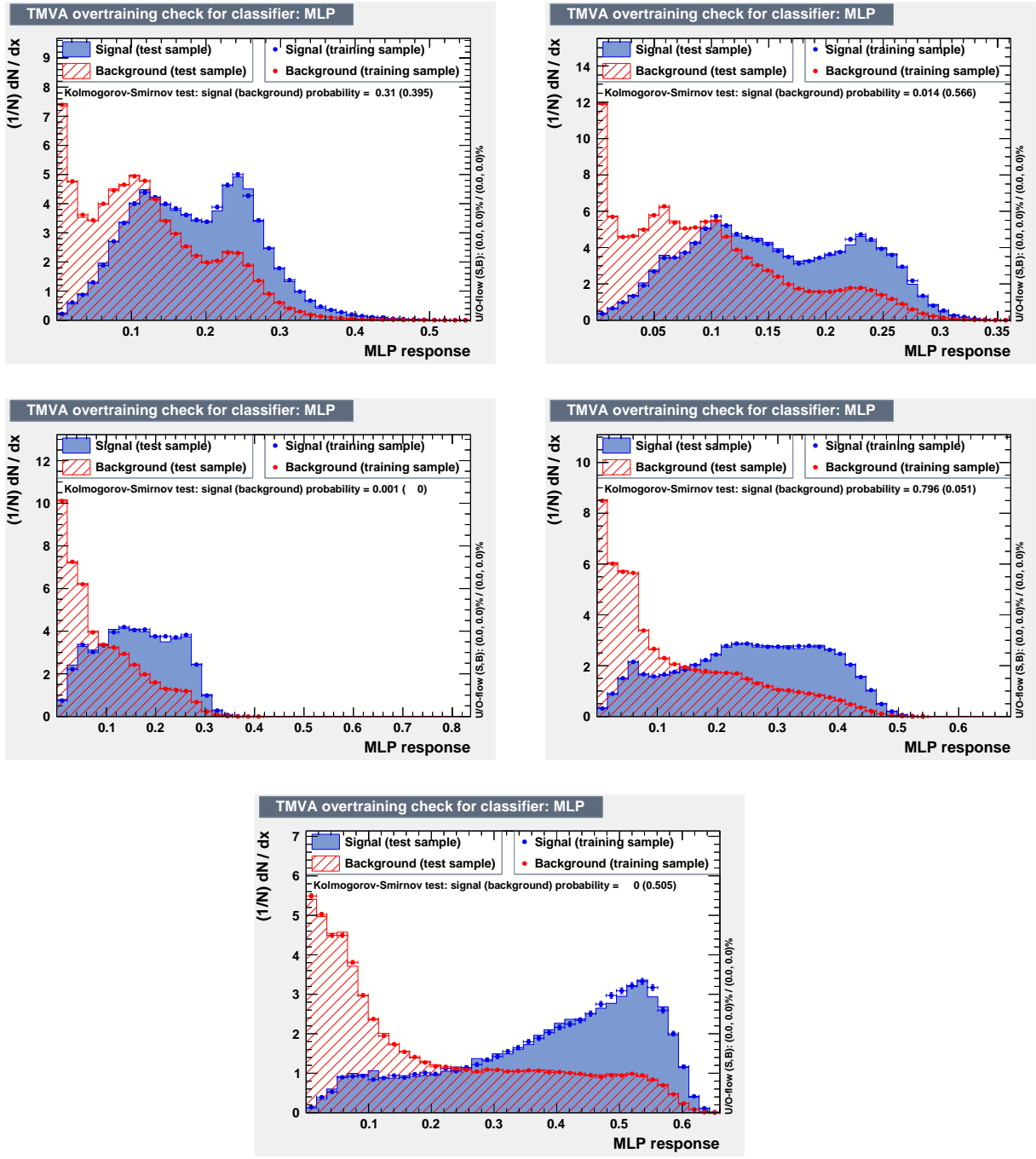
Figure 3.10: Overlapping distributions of signal and background response functions, obtained by applying the MLP method to training and testing samples separately. The results are not affected by overtraining.

Typically, we don't known how many epochs are necessary to achieve a sufficiently good training of the neural network beforehand. We say that a model reaches convergence when additional training on the current data will not improve the model. Figures 3.11 show the convergence test for neural networks for each p_T interval, separately. They represent the MLP error-function convergence versus the training epoch for training and testing results. After some initial fluctuations, all the error estimators tend to stabilize towards a final value. The fact that the difference between the estimators for training and test samples remains consistant means that the results are not effected by overtraining.
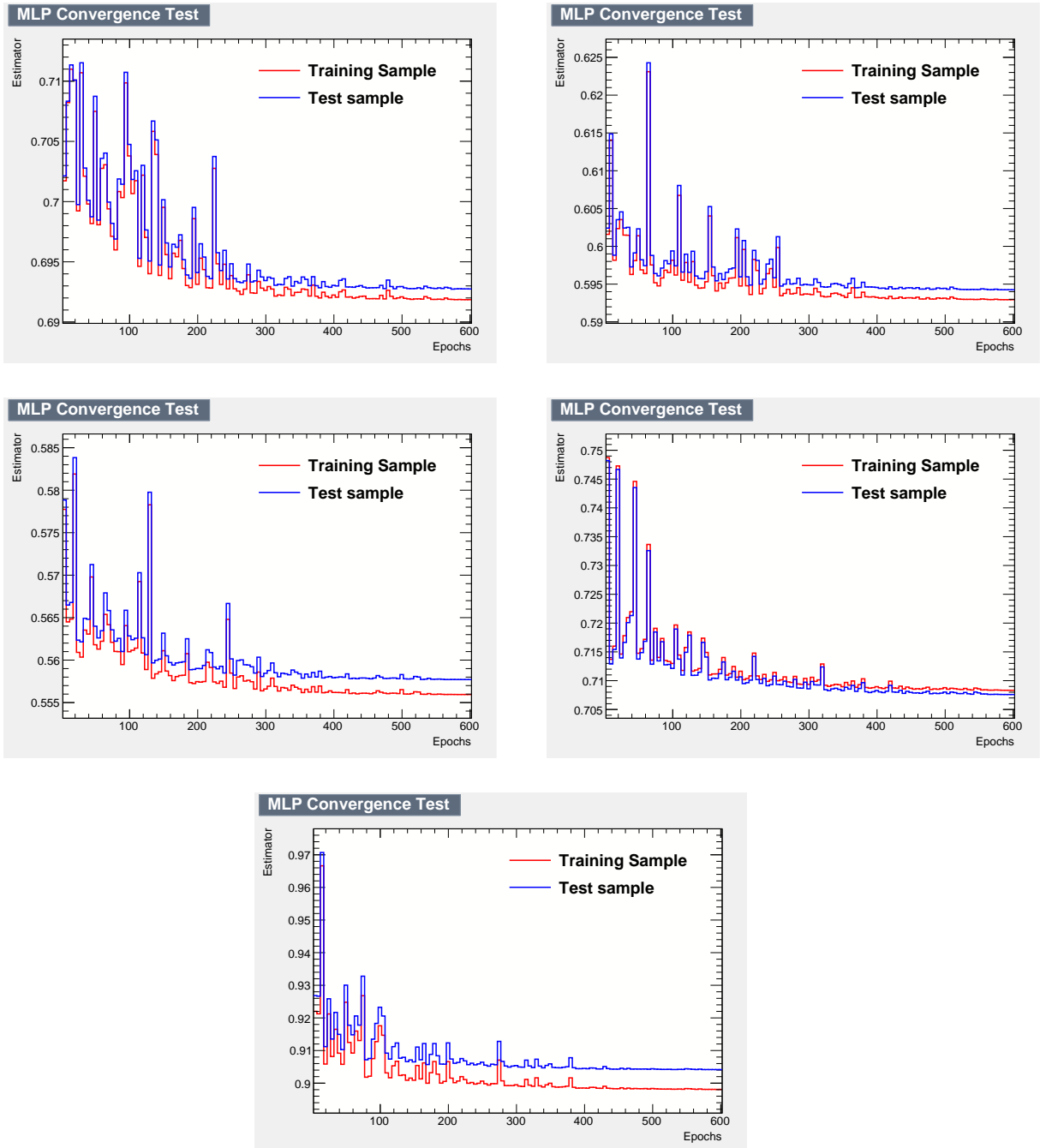

Figure 3.11: MLP convergence test.

A visualization of multilayer perceptron is shown in figure 3.12. The input variables are labelled as layer 0, while layer 1 corresponds to the first hidden layer. The connections between the nodes of the different levels are represented with a color and thickness which are proportional to the weight that the starting node has on the arrival node. All the nodes in the hidden layer contribute to the output.
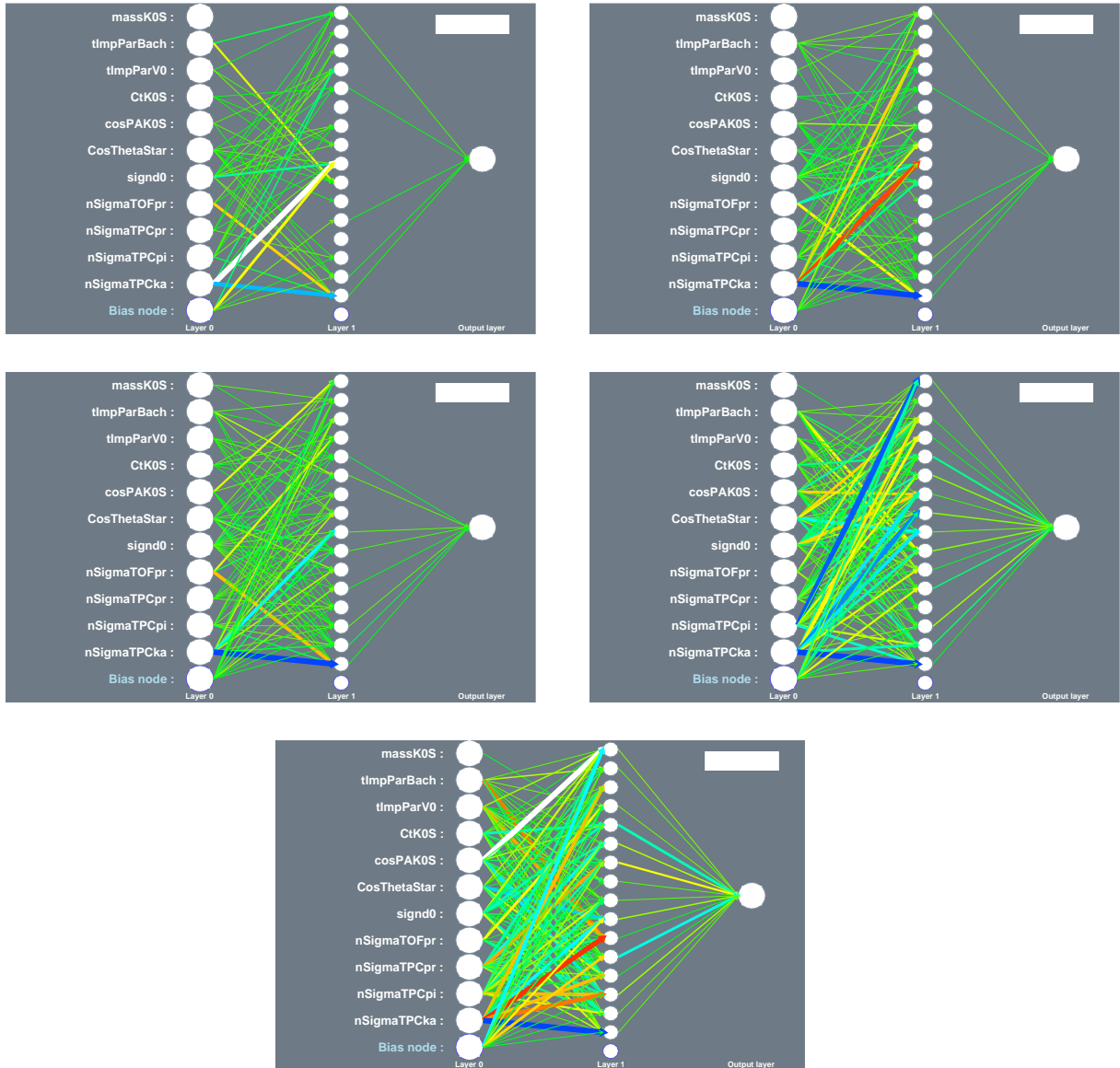

Figure 3.12: Visualization of the multilayer perceptron.

Ranking the input variables means sorting them with criterias of importance and weight that they have within the training process. The MLP neural networks implemented a variable ranking that uses the sum of the weights-squares of the connections between the variable neuron in the input layer and the first hidden layer. Tables 3.5-3.9 illustrate the MLP variable ranking for each p_T interval. As expected, the rankings reflect the same characteristics shown in figures 3.12.

Rank	Variable	Importance
1	nSigmaTPCka	2.746e+02
2	nSigmaTOFpr	1.278e+02
3	signd0	1.186e+02
4	nSigmaTPCpi	3.576e+01
5	cosPAK0S	1.521e+01
6	CtK0S	1.117e+01
7	CosThetaStar	6.519e+00
8	nSigmaTPCpr	4.510e+00
9	tImpParBach	4.739e-01
10	massK0S	2.123e-01
11	tImpParV0	1.362e-01

Table 3.5: Ranking of input variables in the p_T interval [3-4] GeV/c.

Rank	Variable	Importance
1	nSigmaTPCka	3.645e+02
2	nSigmaTOFpr	1.533e+02
3	signd0	9.970e+01
4	nSigmaTPCpi	5.238e+01
5	cosPAK0S	4.892e+01
6	CosThetaStar	1.515e+01
7	CtK0S	1.438e+01
8	nSigmaTPCpr	5.252e+00
9	massK0S	2.549e-01
10	tImpParBach	1.346e-01
11	tImpParV0	6.697e-02

Table 3.6: Ranking of input variables in the p_T interval [4-5] GeV/c.

Rank	Variable	Importance
1	nSigmaTPCka	2.027e+02
2	nSigmaTOFpr	1.217e+02
3	cosPAK0S	5.137e+01
4	signd0	4.863e+01
5	nSigmaTPCpi	4.308e+01
6	CosThetaStar	1.658e+01
7	CtK0S	1.472e+01
8	nSigmaTPCpr	4.096e+00
9	massK0S	7.054e-01
10	tImpParBach	1.395e-01
11	tImpParV0	7.933e-02

Table 3.7: Ranking of input variables in the p_T interval [5-6] GeV/c.

Rank	Variable	Importance
1	nSigmaTPCka	7.411e+01
2	signd0	6.901e+01
3	nSigmaTPCpi	5.637e+01
4	cosPAK0S	4.662e+01
5	CosThetaStar	2.805e+01
6	nSigmaTOFpr	2.188e+01
7	CtK0S	1.329e+01
8	nSigmaTPCpr	4.244e+00
9	massK0S	1.966e-01
10	tImpParV0	1.155e-01
11	tImpParBach	1.070e-01

Table 3.8: Ranking of input variables in the p_T interval [6-8] GeV/c.

Rank	Variable	Importance
1	cosPAK0S	6.122e+01
2	signd0	4.075e+01
3	nSigmaTPCka	2.162e+01
4	nSigmaTOFpr	1.651e+01
5	CtK0S	1.511e+01
6	CosThetaStar	1.264e+01
7	nSigmaTPCpi	1.195e+01
8	nSigmaTPCpr	7.135e+00
9	massK0S	2.320e-01
10	tImpParV0	1.840e-01
11	tImpParBach	8.723e-02

Table 3.9: Ranking of input variables in the p_T interval [8-10] GeV/c.

By TMVA convention, signal (background) events accumulate at large (small) classifier output values. Hence, cutting on the output and retaining the events with larger classifier outputs than the cut requirement selects signal samples with efficiencies and purities that respectively decrease and increase with the cut value. Figure 3.13 shows the signal (solid blue line) and background (solid red line) efficiencies versus the cut value applied to a MLP output. The solid green line in the plots represents the significance defined as $S/\sqrt{S+B}$, with S and B respectively number of signal and background events.
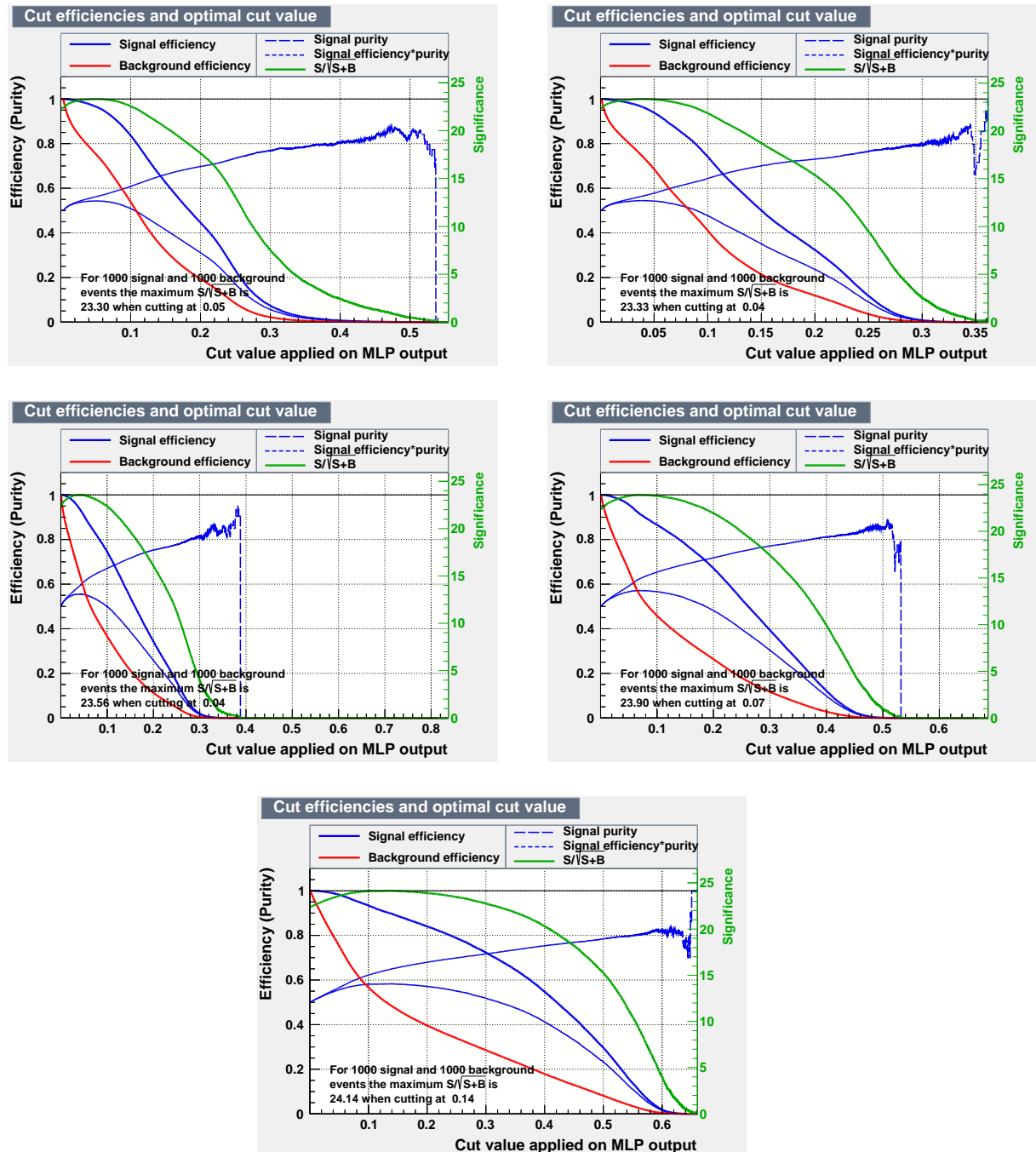

Figure 3.13: Signal and background efficiency with relative to any possible cutting value.

Figure 3.14 shows the Receiver Operating Characteristic (ROC) curves, showing the background rejection over the signal efficiency of the remaining sample, for each p_T bin.
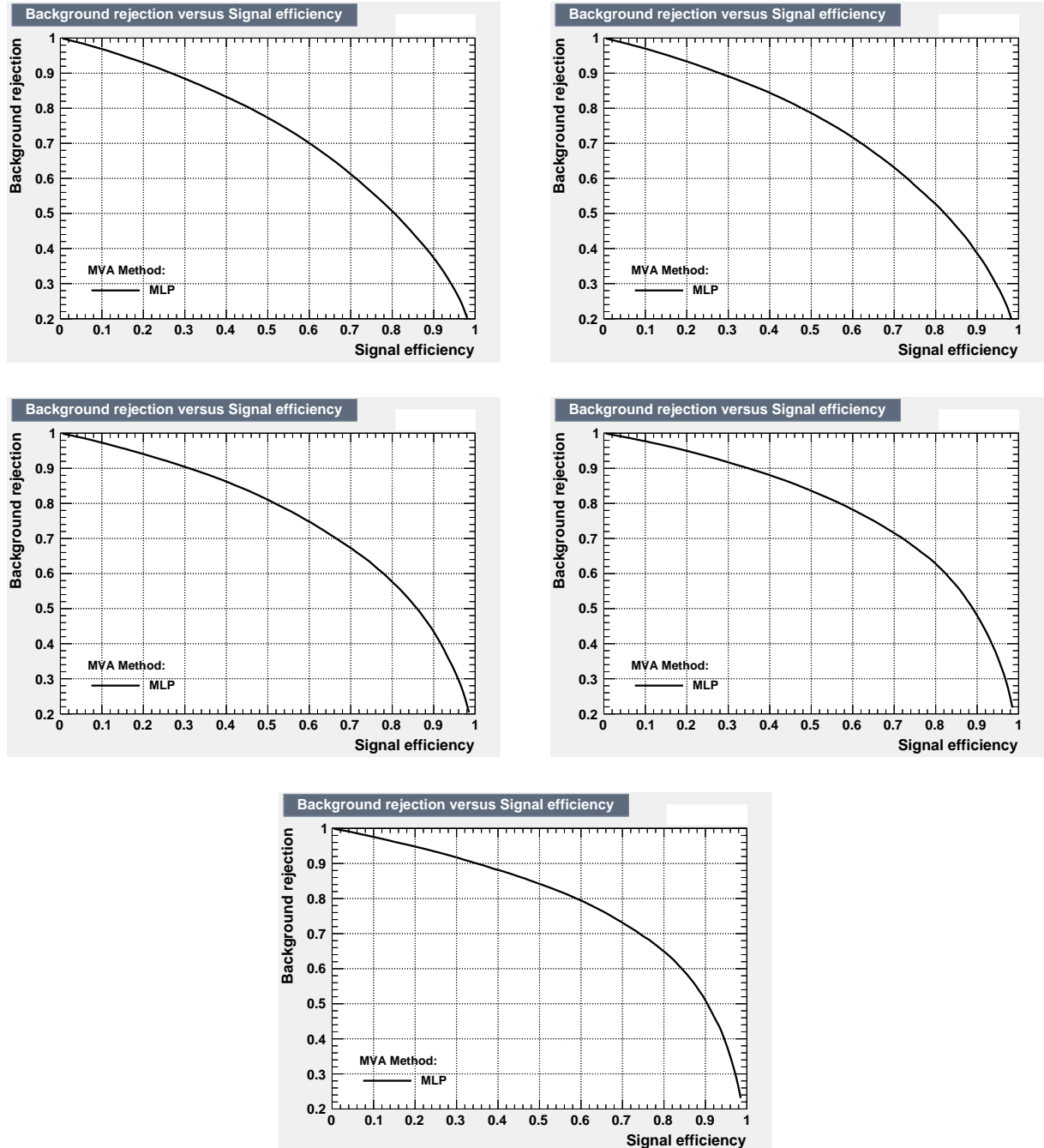

Figure 3.14: ROC curves. To a greater efficiency of the signal corresponds a smaller amount of background which is rejected.

3.6   Running the MLP algorithm on a test sample

In order to verify the proper functioning of the trained MLP algorithm, we prepare a dedicated test sample (called validation sample) built with real candidates, taken by the ALICE experiment during the 2018 Pb-Pb data taking campaign, where a sample of simulated Λ_c was injected. The signal candidates were extracted from a completely independent MC simulation from the one used in the training of the MLP algorithm, to avoid any bias in the test. The number of signal candidates injected in each p_T interval is shown in figure 3.15, where the mean and the width of the Gaussian fit of the Λ_c peak are reported. After running the MLP algorithm on the data, five different cuts on the MLP response function were applied to extract the invariant mass distribution: 0, 0.05, 0.1, 0.15 and 0.2. Then, the signal extraction was performed via a fit of the invariant mass distribution in each p_T interval. A Gaussian function was used to model the signal peak, and a 2nd order polynomial function was used to model the background. To avoid statistical fluctuation, the width of the Gaussian fit was fixed to MC expectations. The invariant mass distributions of Λ_c candidates with the corresponding fit functions are shown in figures 3.21-3.25 (to the left - background fit function is superimposed to the invariant mass distribution; to the right - the Gaussian fit of the background-subtracted distribution) for each of the five applied cuts. The signal and background values used to calculate the signal-to-background ratio are obtained considering a 3σ range with respect to the mean of the Gaussian fit. The cut on the MLP response allows reducing the background below the Λ_c peak but also leads to a rejection of a certain fraction of signal candidates; to evaluate the signal injected in each p_T bin in the correct way, such rejection has to be taken into account accordingly. This was done by counting the fraction of the Λ_c signal candidates rejected in the testing sample by the selection on the classifier output. The efficiencies in the five p_T intervals for each of the five cut values applied to the MLP output are reported in table 3.10. Since the amount of signal candidates injected in each p_T interval is known, a comparison between this number and the signal which is extracted with the fitting procedure and corrected by the classifier efficiency allows a direct verification of the full method. Such a comparison is shown in figures 3.16-3.20 for each p_T interval and shows that the corrected signals are compatible within the statistical uncertanties with the expected value.
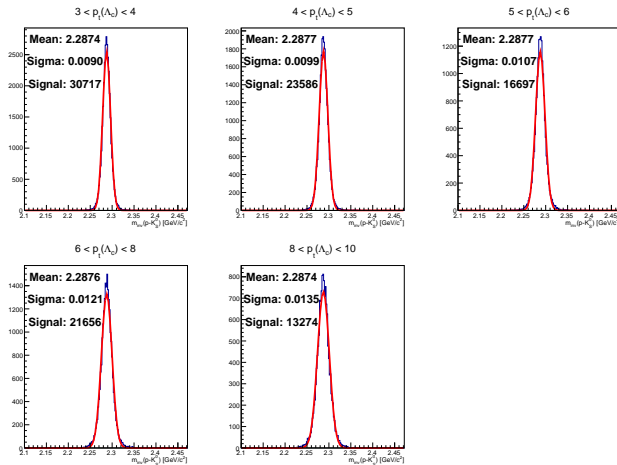

Figure 3.15: Λ_c signal candidates from Monte Carlo simulations injected into the validation sample.
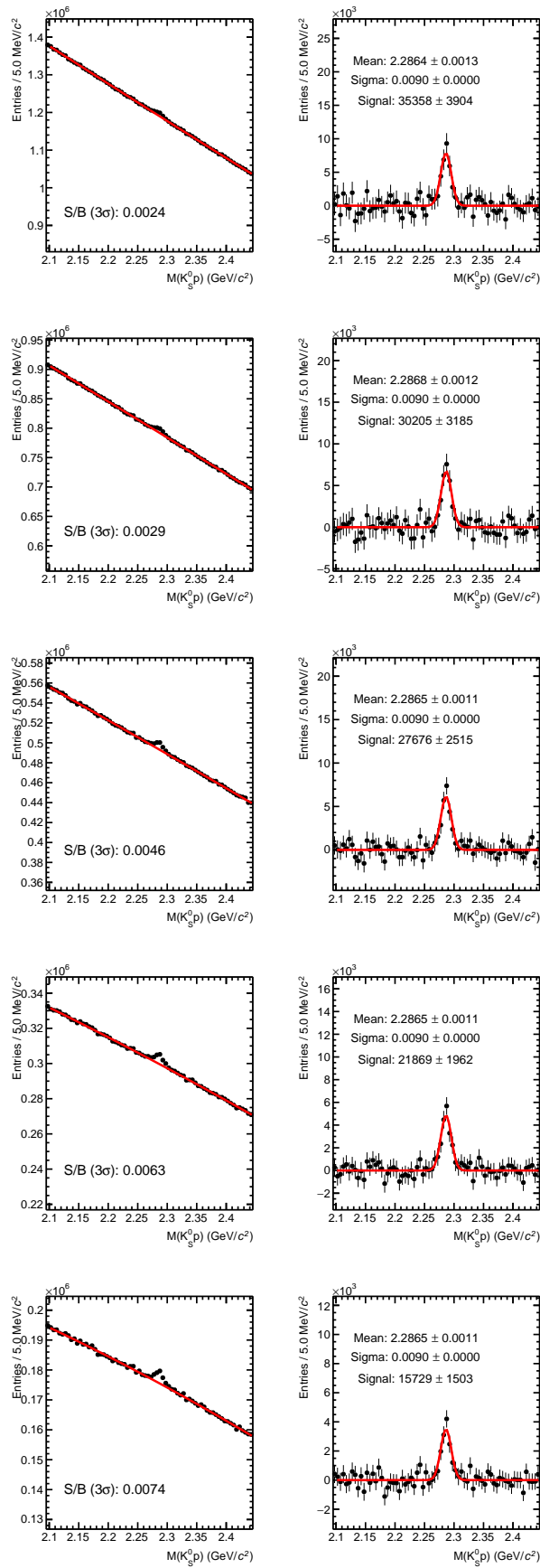
Figure 3.16: Invariant mass distribution of Λ_c candidates with fit functions in the p_T interval [3-4] GeV/c for each of the five applied cuts (from top to bottom): 0.0, 0.05, 0.1, 0.15, 0.2.
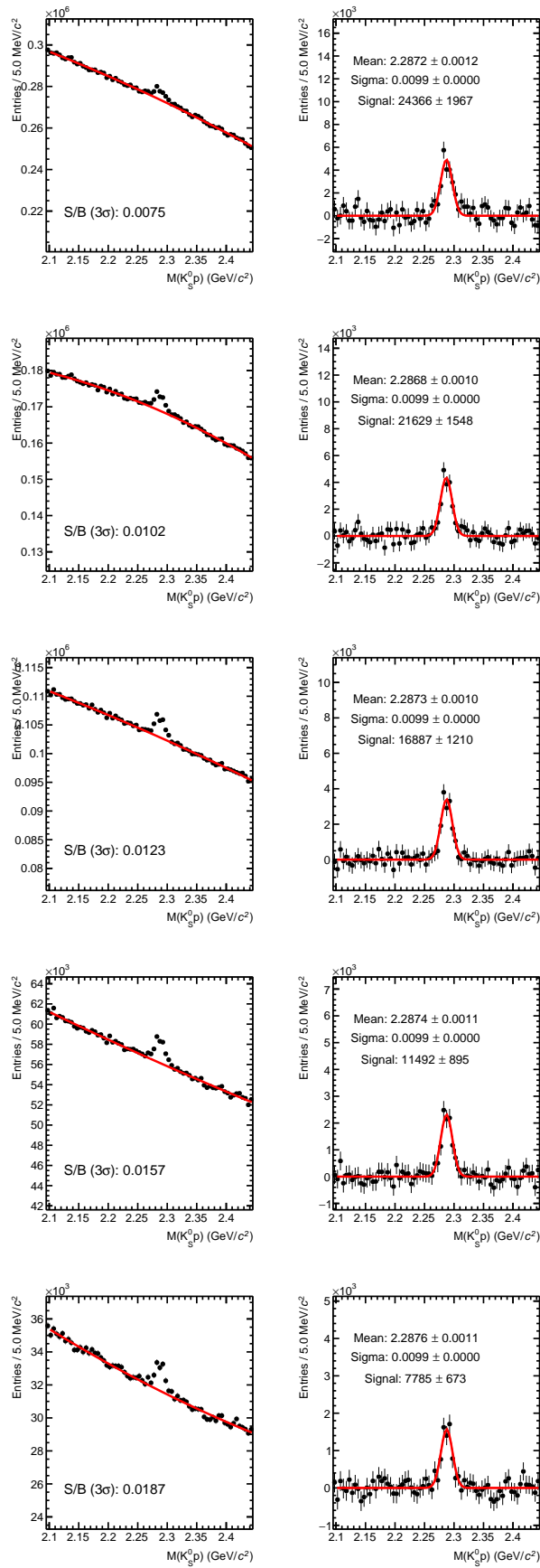
Figure 3.17: Invariant mass distribution of Λ_c candidates with fit functions in the p_T interval [4-5] GeV/c for each of the five applied cuts (from top to bottom): 0.0, 0.05, 0.1, 0.15, 0.2.
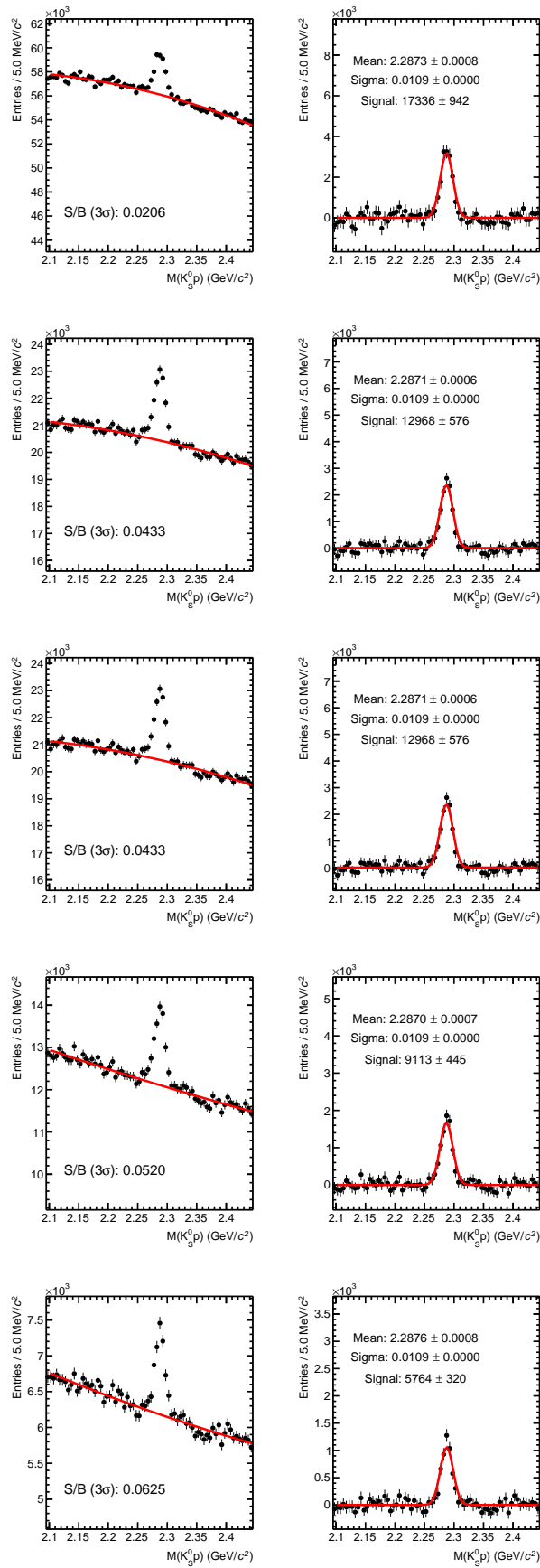
Figure 3.18: Invariant mass distribution of Λ_c candidates with fit functions in the p_T interval [5-6] GeV/c for each of the five applied cuts (from top to bottom): 0.0, 0.05, 0.1, 0.15, 0.2.
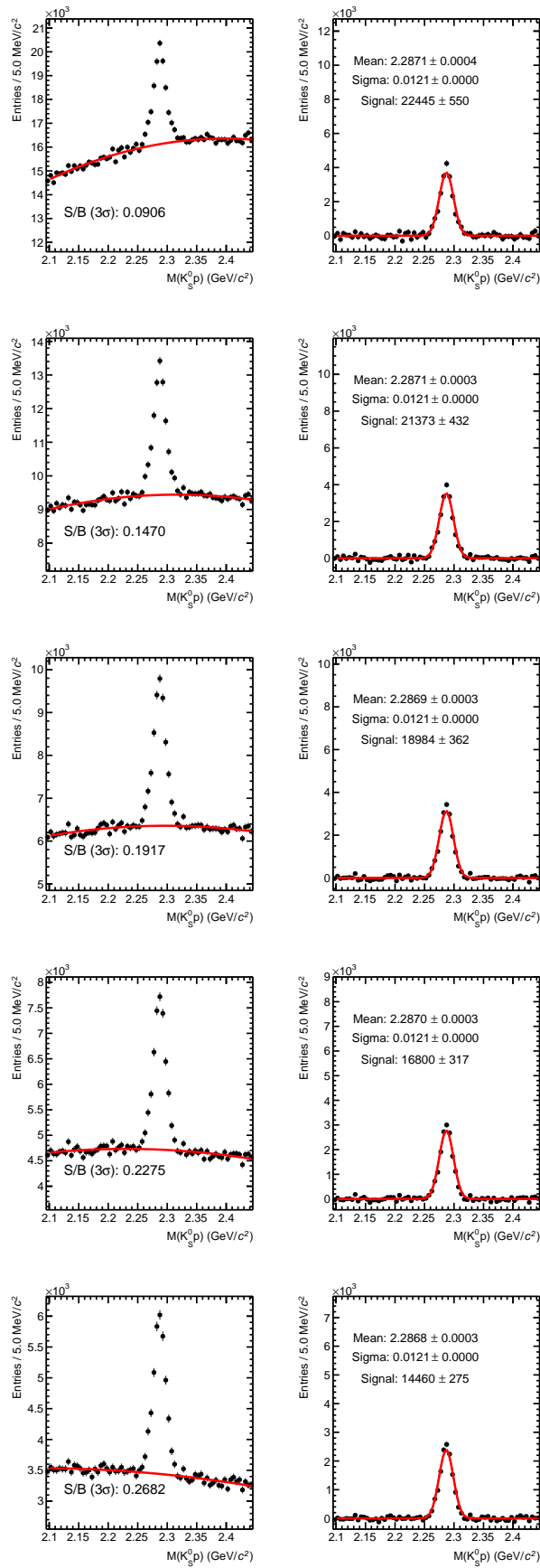
Figure 3.19: Invariant mass distribution of Λ_c candidates with fit functions in the p_T interval [6-8] GeV/c for each of the five applied cuts (from top to bottom): 0.0, 0.05, 0.1, 0.15, 0.2.
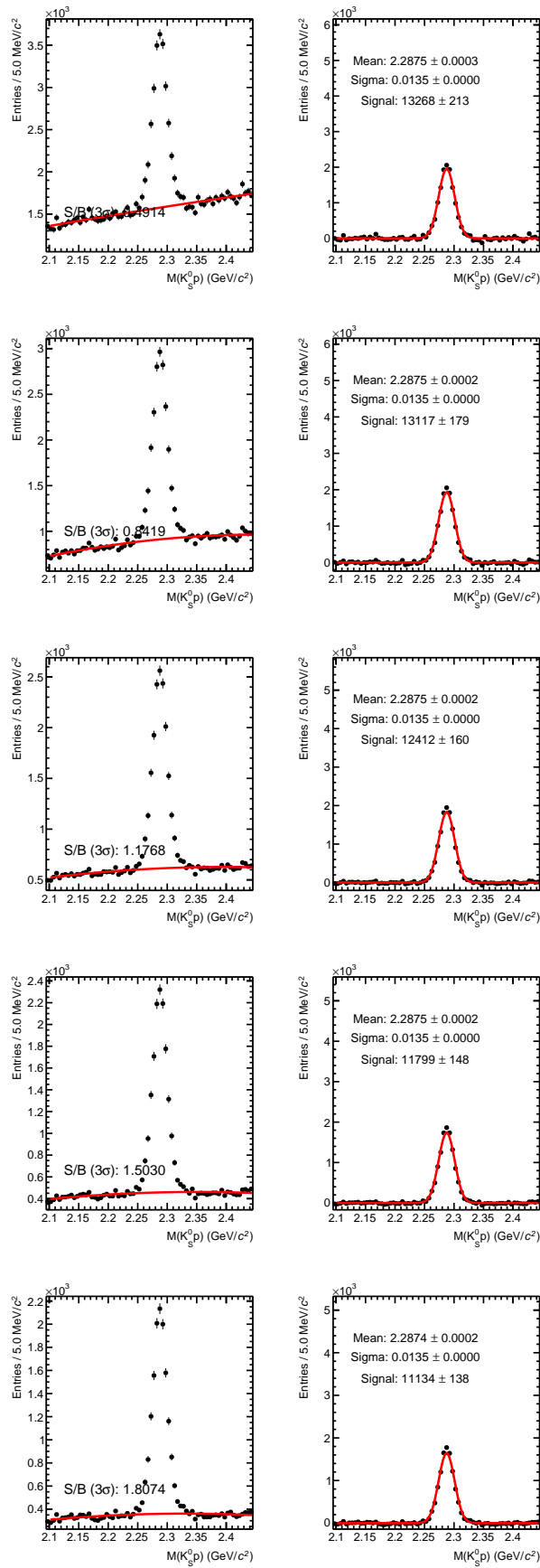
40

Figure 3.20: Invariant mass distribution of Λ_c candidates with fit functions in the p_T interval [8-10] GeV/c for each of the five applied cuts (from top to bottom): 0.0, 0.05, 0.1, 0.15, 0.2.

Cuts	Λ_c p_T bin GeV/c				
	$3-4$	$4-5$	$5-6$	$6-8$	$8-10$
0	1	1	1	1	1
0.05	(0.966±0.001)	(0.938± 0.001)	(0.906±0.001)	(0.957±0.001)	(0.982±0.001)
0.1	(0.836±0.001)	(0.741±0.002)	(0.746±0.002)	(0.866±0.001)	(0.934±0.001)
0.15	(0.625±0.002)	(0.501±0.002)	(0.541±0.002)	(0.780±0.002)	(0.888±0.002)
0.2	(0.446±0.002)	(0.323±0.002)	(0.343±0.002)	(0.671±0.002)	(0.840±0.002)

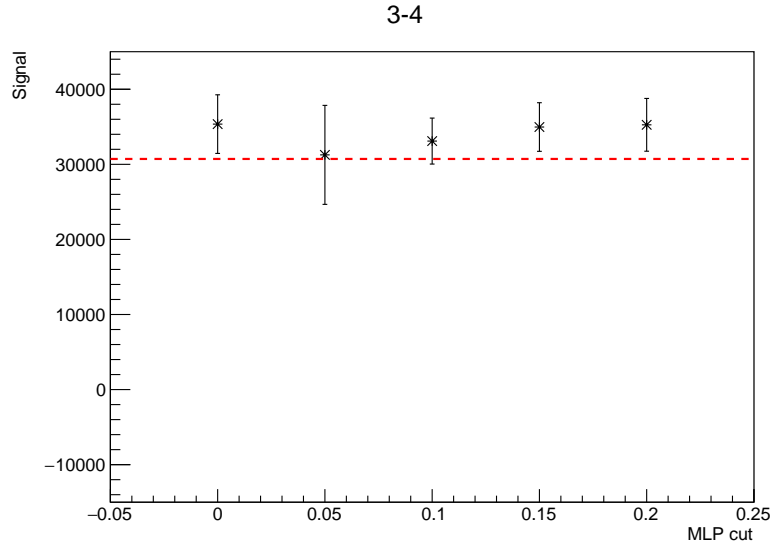Table 3.10: Efficiencies for each p_T bin corresponding to every cut.

Figure 3.21: Corrected signals as a function of the cutting point on the MLP response. The dashed line represents the injected MLP signal. This plot corresponds to $p_T(\Lambda_c)$ in the interval [3-4] GeV/c.

Figure 3.22: Corrected signals as a function of the cutting point on the MLP response. The dashed line represents the injected MLP signal. This plot corresponds to $p_T(\Lambda_c)$ in the interval [4-5] GeV/c.
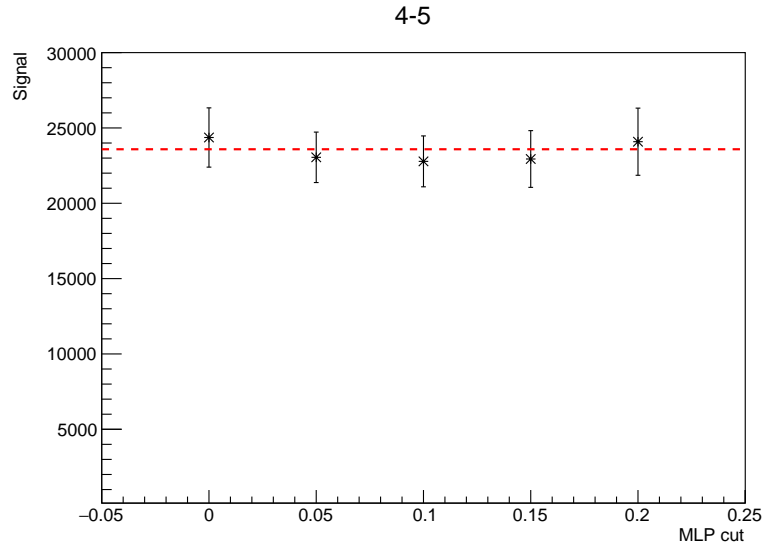

Figure 3.23: Corrected signals as a function of the cutting point on the MLP response. The dashed line represents the injected MLP signal. This plot corresponds to $p_T(\Lambda_c)$ in the interval [5-6] GeV/c.

Figure 3.24: Corrected signals as a function of the cutting point on the MLP response. The dashed line represents the injected MLP signal. This plot corresponds to $p_T(\Lambda_c)$ in the interval [6-8] GeV/c.
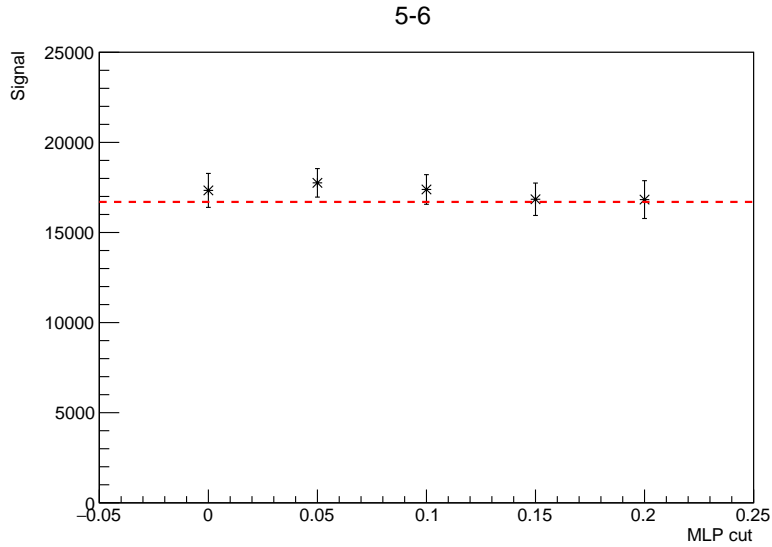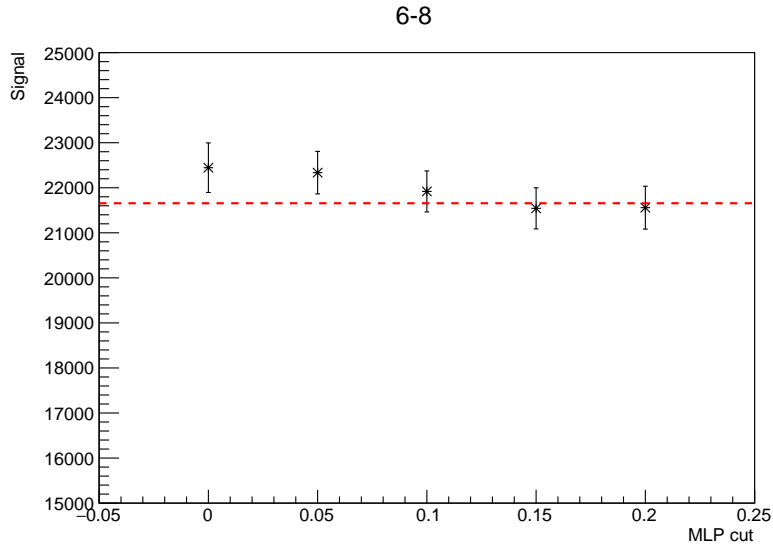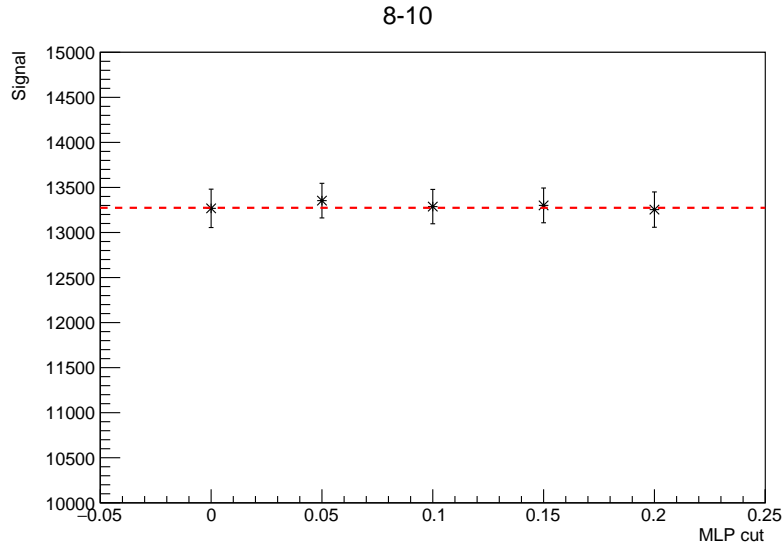

Figure 3.25: Corrected signals as a function of the cutting point on the MLP response. The dashed line represents the injected MLP signal. This plot corresponds to $p_T(\Lambda_c)$ in the interval [8-10] GeV/c.

Conclusions

In this thesis, a feasibility study on the reconstruction of the Λ_c baryon with artificial neural networks was presented. When dealing with complicated analisis such as this one on the Λ_c charmed baryon, the use of machine learning techniques ends up being indispensable. Machine learning applications are progressively expanding in high energy physics, where the signals to be investigated are usually hard to extract due to the high background. These techniques allow us to consider several variables of a single event at the same time and to subsequently classify all the analyzed events on the basis of regularities that the selected algorithm learns directly from the data. This study used the ROOT-integrated TMVA toolkit which hosts a large variety of multivariate classification algorithms. Among them, artificial neural networks have proven to be very effective in solving complex problems as the one considered in this thesis, where the short decay length and the low signal-to-background ratio of the Λ_c makes the signal extraction very challenging. The artificial neural network class chosen for the present work is the multilayer perceptron (MLP), where the complexity of the network can be reduced by organizing the neurons in layers and only allowing direct connections from a given layer to the following layer. The TMVA package provides automatic tools for training, testing and evaluating the performance of the classification methods used. The MLP algorithm was trained with simulated Λ_c signal candidates and with data taken by the ALICE experiment for background candidates, and then applied on a validation sample where the number of true Λ_c is known. It has been shown that by applying progressively larger cuts on the MLP output it is possible to increase the signal-to-background ratio; moreover, the corrected result is always compatible with the injected signal within the statistical uncertainties, proving that the method can be safely applied and provides an unbiased result.

Bibliography

[1] Sutton, Christine. *Quantum chronodynamics.* Enciclopaedia Britannica. 15/11/2018. https://www.britannica.com/science/quantum-chromodynamics

[2] K.J. Eskola, K. Kajantie, P.V. Ruuskanene and K. Tuominen, *Scaling of transverse energies and multiplicities with atomic number and energy in ultrarelativistic nuclear collisions*, Nucl. Phys. B, 570, [arXiv:hep-ph/9909456], 2000

[3] A. Andronic, *An overview of the experimental study of quark-gluon matter in highenergy nucleus-nucleus collisions*, [arXiv:nucl-ex/1407.5003], 2014

[4] Barbara Guerzoni. *Identified primary hadron spectra with the TOF detector of the ALICE experiment at LHC* PhD thesis, Alma Mater Studiorum, Università di Bologna, 2012

[5] J. Rafelski, B. Müller, *Strangeness production in the quark-gluon plasma*, Phys.Rev.Lett.48(1982)1066

[6] Sarkar, Sourav, Satz, Helmut Sinha, Bikash (Ed.). (2010). *The physics of the quark-gluon plasma Introductory lectures.* Germany: Springer.

[7] ALICE Collaboration *Centrality dependence of the nuclear modification factor of charged pions, kaons, and protons in Pb-Pb collisions at $\sqrt{s_{NN}}$ = 2.76 TeV.* arXiv:1506.07287v3

[8] The ALICE Experiment. *A Large Ion Collider Experiment.* 16/11/2018 http://aliceinfo.cern.ch/Public/en/Chapter2/

[9] J. Ashkin H. Bethe. *Expeimental Nuclear Physics.* In: a cura di E. Segré. Wiley, 1953

[10] ALICE Collaboration. *Technical Design Report of the Time Projection Chamber.* Rapp. tecn. CERN, 1999

[11] TMVA version 4.2.0 CERN-OPEN-2007-007 *Data Analysis, Statistics and Probability.* March 3, 2017 arXiv:physics/0703039 http:// tmva.sourceforge.net

[12] T. Sjöstrand, S. Mrenna and P.Z. Skands, *PYTHIA 6.4 physics and manual*, JHEP 05 (2006) 026 [hep-ph/0603175]

[13] X.N Wang and M. Gyulassy, *HIJING: a Monte Carlo model for multiple jet production in pp, p-A and A-A collisions*, Phys. Rev. D44 (1991) 3501

[14] R. Brun et al., *GEANT detector description and simulation tool*, CERN-W-5013 (1994)

Ringraziamenti

Ringrazio il Professor Andrea Alici che mi ha accompagnato nella stesura di questa tesi; per il suo tempo dedicato al lavoro e alla disponibilitá nei miei confronti dimostrata sempre con gentilezza. La professionalitá e la dedizione che trasmette mi hanno fatto trovare un ambiente di lavoro ideale che ha reso dedicarmi a questa tesi un piacere.

Ringrazio la Professoressa Gilda Scioli. Anche se non é stata direttamente coinvolta nella realizzazione di questa tesi, vi ha contribuito piú di quanto ne é consapevole. Grazie al sua energia e positivitá, non ha potuto fare a meno di trasmettere il suo entusiasmo verso la sua materia. Non sarei riuscita a immaginare di volermi laureare con una tesi in una materia diversa, e non potrei essere piú felice del percorso scelto.

Ringrazio la mia famiglia, che ha creduto in me, mi ha dato la libertá di scegliere il mio percorso e mi ha sostenuto cercando di darmi tutto quello di cui hanno immaginato avrei potuto avere bisogno. Soprattutto non hanno mai mancato di festeggiare i miei successi.
I miei nonni, che mi hanno dato una casa nel periodo universitario e hanno fatto di tutto al meglio delle loro possibilitá perché io potessi essere piú agevolata possibile nello studio.
I miei parenti vicini e lontani, che mi hanno pensato tanto in questi anni e me hanno tutti cercato a modo loro di aiutarmi e incoraggiarmi.

Ringrazio i miei amici e colleghi, che sono stati indispensabili affinché io arrivassi fin qui. Hanno reso questo dipartimento un posto accogliente in cui é stato piacevole trascorrere momenti di studio che hanno portato a tanti successi e in cui hanno avuto inizio amicizie importanti. Hanno creduto in me, e grazie a loro sapevo di poter sempre trovare aiuto quando ne avevo bisogno e, che ne siano consapevoli o meno, mi hanno insegnato tanto.